



Chapter 6

Kiruna-Type Iron Oxide-Apatite (IOA) and Iron Oxide Copper-Gold (IOCG) Deposits Form by a Combination of Igneous and Magmatic-Hydrothermal Processes: Evidence from the Chilean Iron Belt

Adam C. Simon,^{1,†} Jaayke Knipping,² Martin Reich,³ Fernando Barra,³ Artur P. Deditius,⁴
Laura Bilenker,⁵ and Tristan Childress¹

¹Department of Earth and Environmental Sciences, University of Michigan, 1100 North University Avenue,
Ann Arbor, Michigan 48109-1005

²Institut für Mineralogie, Leibniz Universität Hannover, Callinstraße 3, 30167, Hannover, Germany

³Department of Geology and Andean Geothermal Center of Excellence (CEGA), FCFM, Universidad de Chile,
Plaza Ercilla 803, Santiago, Chile

⁴School of Engineering and Information Technology, Murdoch University, 90 South Street, Murdoch, Western Australia 6150, Australia

⁵Department of Earth, Ocean, and Atmospheric Sciences, 2020–2207 Main Mall, University of British Columbia,
Vancouver, British Columbia, Canada V6T 1Z4

Abstract

Iron oxide copper-gold (IOCG) and Kiruna-type iron oxide-apatite (IOA) deposits are commonly spatially and temporally associated with one another, and with coeval magmatism. Here, we use trace element concentrations in magnetite and pyrite, Fe and O stable isotope abundances of magnetite and hematite, H isotopes of magnetite and actinolite, and Re-Os systematics of magnetite from the Los Colorados Kiruna-type IOA deposit in the Chilean iron belt to develop a new genetic model that explains IOCG and IOA deposits as a continuum produced by a combination of igneous and magmatic-hydrothermal processes. The concentrations of [Al + Mn] and [Ti + V] are highest in magnetite cores and decrease systematically from core to rim, consistent with growth of magnetite cores from a silicate melt, and rims from a cooling magmatic-hydrothermal fluid. Almost all bulk $\delta^{18}\text{O}$ values in magnetite are within the range of 0 to 5‰, and bulk $\delta^{56}\text{Fe}$ for magnetite are within the range 0 to 0.8‰ of Fe isotopes, both of which indicate a magmatic source for O and Fe. The values of $\delta^{18}\text{O}$ and δD for actinolite, which is paragenetically equivalent to magnetite, are, respectively, 6.46 ± 0.56 and -59.3 ± 1.7 ‰, indicative of a mantle source. Pyrite grains consistently yield Co/Ni ratios that exceed unity, and imply precipitation of pyrite from an ore fluid evolved from an intermediate to mafic magma. The calculated initial $^{187}\text{Os}/^{188}\text{Os}$ ratio (Os_i) for magnetite from Los Colorados is 1.2, overlapping Os_i values for Chilean porphyry-Cu deposits, and consistent with an origin from juvenile magma. Together, the data are consistent with a geologic model wherein (1) magnetite microlites crystallize as a near-liquidus phase from an intermediate to mafic silicate melt; (2) magnetite microlites serve as nucleation sites for fluid bubbles and promote volatile saturation of the melt; (3) the volatile phase coalesces and encapsulates magnetite microlites to form a magnetite-fluid suspension; (4) the suspension scavenges Fe, Cu, Au, S, Cl, P, and rare earth elements (REE) from the melt; (5) the suspension ascends from the host magma during regional extension; (6) as the suspension ascends, originally igneous magnetite microlites grow larger by sourcing Fe from the cooling magmatic-hydrothermal fluid; (7) in deep-seated crustal faults, magnetite crystals are deposited to form a Kiruna-type IOA deposit due to decompression of the magnetite-fluid suspension; and (8) the further ascending fluid transports Fe, Cu, Au, and S to shallower levels or lateral distal zones of the system where hematite, magnetite, and sulfides precipitate to form IOCG deposits. The model explains the globally observed temporal and spatial relationship between magmatism and IOA and IOCG deposits, and provides a valuable conceptual framework to define exploration strategies.

Introduction

Iron oxide copper-gold (IOCG) deposits (e.g., Olympic Dam), and iron oxide-apatite (IOA) deposits (e.g., Kiruna-type) deposits are important sources of their namesake metals, as well as rare earth elements (REE), U, P, Ag, Co, Bi, and Nb that are economically important by-products in some deposits (Hitzman et al., 1992; Foose and McLelland, 1995; Hitzman, 2000; Williams et al., 2005; Chiaradia et al., 2006; Corriveau, 2007; Barton, 2014). Both deposit types occur globally and

range in age from Late Archean to Plio-Pleistocene (Barton and Johnson, 1996; Naslund et al., 2002). Titanium-poor magnetite modally dominates Kiruna-type IOA deposits, distinguishing them from nelsonites, whereas magnetite and (specular) hematite modally dominate IOCG deposits (Williams et al., 2005). Both deposit types contain metal sulfides but only reach economic grades in IOCG deposits. Reported (premining) resources for Kiruna-type deposits range from tens to ~2,500 million metric tons (Mt) for the namesake Kiirunavaara deposit in Kiruna, Sweden, and grades reach as high as 50% Fe. Reported resources for IOCG deposits range from tens to ~2,000 Mt for the Olympic Dam, and Cu

[†] Corresponding author: e-mail, simonac@umich.edu

and Au grades are similar to, and commonly exceed, those in porphyry-type deposits (Williams et al., 2005).

Generally, there seems to be consensus that IOCG deposits formed by hydrothermal processes resulting in styles of mineralization that include structurally controlled veins and breccias, as well as disseminations and massive lenses (Ruiz and Erickson, 1962; Sillitoe, 2003; Williams et al., 2005; Mumin et al., 2007; Groves et al., 2010; Barton, 2014). However, a common source of the hydrothermal ore fluid responsible for the formation of IOCG deposits remains unconstrained, with evidence supporting the presence of meteoric, evaporitic, and magmatic-hydrothermal fluids (Williams et al., 2005; Barton, 2014). In contrast, there is no consensus for the origin of Kiruna-type deposits, which exhibit varied styles of mineralization that include discordant breccias, dikes, veins, and massive tabular bodies, as well as disseminations in permeable volcano-sedimentary host rocks (Sillitoe, 2003; Williams et al., 2005; Barton, 2014). Working hypotheses for the formation of Kiruna-type deposits include formation by meteoric or metamorphic hydrothermal fluids that scavenge metals from intermediate to mafic host rocks (Menard, 1995; Rhodes and Oreskes, 1999; Barton and Johnson, 1996, 2004; Haynes et al., 1995; Rhodes et al., 1999; Haynes, 2000; Sillitoe and Burrows, 2002; Dare et al., 2015), and magmatic-hydrothermal fluids that scavenge metals directly from magma (Pollard, 2006; Westhues et al., 2016, 2017a, b). A pure igneous hypothesis includes liquid immiscibility, wherein a parent silicate melt of intermediate to mafic composition separates into immiscible, Fe-P-rich, Si-poor melt, and Si-rich, Fe-P-poor melt, followed by coalescence and physical separation of the Fe-P-rich melt to form an iron oxide-apatite orebody (Park, 1961; Nyström and Henríquez, 1994; Trivisany et al., 1995; Naslund et al., 2002; Henríquez et al., 2003; Chen et al., 2010; Tornos et al., 2016, 2017; Velasco et al., 2016; Hou et al., 2018).

In many districts, Kiruna-type deposits are spatially and temporally associated with IOCG deposits, such as in the Chilean iron belt (Fig. 1; Sillitoe, 2003) and Missouri, United States (Seeger, 2000, 2003; Day et al., 2016). Drill core and geophysical data indicate that the spatial relationship is commonly a function of depth, where IOCG mineralization at shallow paleodepths transitions with depth to sulfide-poor, Kiruna-type mineralization (Fig. 2; Espinoza et al., 1996; Sillitoe, 2003; Williams et al., 2005). This observation of a structurally controlled, vertical continuum, has led many to hypothesize that the two deposit types are part of a single ore-forming system (Sillitoe, 2003; Williams et al., 2005; Day et al., 2016; Barra et al., 2017). Supporting this hypothesis are temperatures of mineralization obtained from fluid inclusion microthermometry and mineral-mineral stable isotope thermometry that indicate that Kiruna-type mineralization formed at higher temperatures relative to IOCG mineralization (Williams et al., 2005; Barton, 2014). Reported temperatures of mineralization are ~500° to >650°C for Kiruna-type deposits, 400° to 550°C for magnetite, and 300° to 400°C for hematite and sulfides in IOCG deposits (Williams et al., 2005). Thus, the hydrothermal models invoked for both deposit types allow for a downtemperature genetic connection, notwithstanding the lack of consensus for the source of the hydrothermal fluid.

It is more difficult to reconcile the liquid immiscibility model for the formation of both deposit types (Naslund et

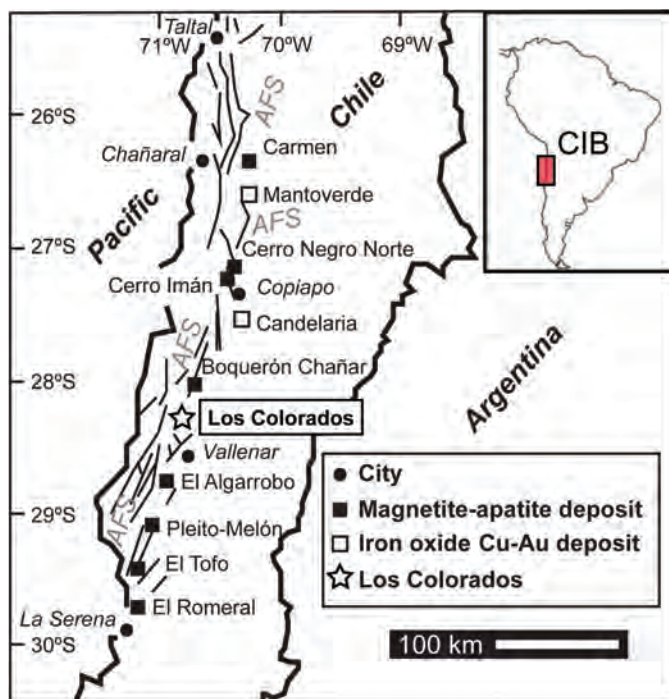


Fig. 1. Map of the Chilean iron belt (CIB), showing the spatial association of Kiruna-type iron oxide-apatite (IOA) and iron oxide copper-gold (IOCG) deposits. The Los Colorados Kiruna-type IOA is highlighted. Modified from Knipping et al. (2015a). AFS = Atacama fault system.

al., 2002; Tornos et al., 2016). In a comprehensive review of experimental data, Lindsley and Epler (2017) report that there is no plausible experimental evidence for the existence of Ti-rich, Fe-Ti oxide melts at geologically reasonable temperatures. Lindsley and Epler (2017) discuss all published datasets that assess the ability for various fluxes, for example, apatite, fluorine, and carbon, to stabilize Fe-Ti oxide melts in natural systems. Those authors conclude that Fe-Ti oxide bodies that have crosscutting relationships with their host rocks cannot have formed by liquid immiscibility. Lindsley and Epler (2017) point out that experimental data from Lester et al. (2013a), and recent experimental data published by Hou et al. (2018), which have been cited to support liquid immiscibility as a viable geologic process (e.g., Tornos et al., 2016), contain sulfur and phosphorus concentrations far in excess of natural silicate melts. Importantly, Lester et al. (2013a) did not measure the water concentration in the immiscible Fe- and Si-rich melts in their experimental charges and, thus, those experiments provide no information about the ability of water to reduce the density of an immiscible Fe-rich melt. Based on data and discussion in Lindsley and Epler (2017) and our own appraisal, we suggest workers stop referring to Lester et al. (2013a)—in particular in terms of the unsupported evidence of water preferentially partitioning into the Fe-rich melt—as evidence for the existence of Fe-Ti liquid immiscibility in Kiruna-type systems. The preferential partitioning of water into Fe-rich melt has now, in fact, been disproven. Hou et al. (2018) used Raman spectroscopy to measure the concentration of H₂O in experimentally produced, coexisting Fe-rich and Fe-poor silicate melts (glasses) and report that water partitions preferentially

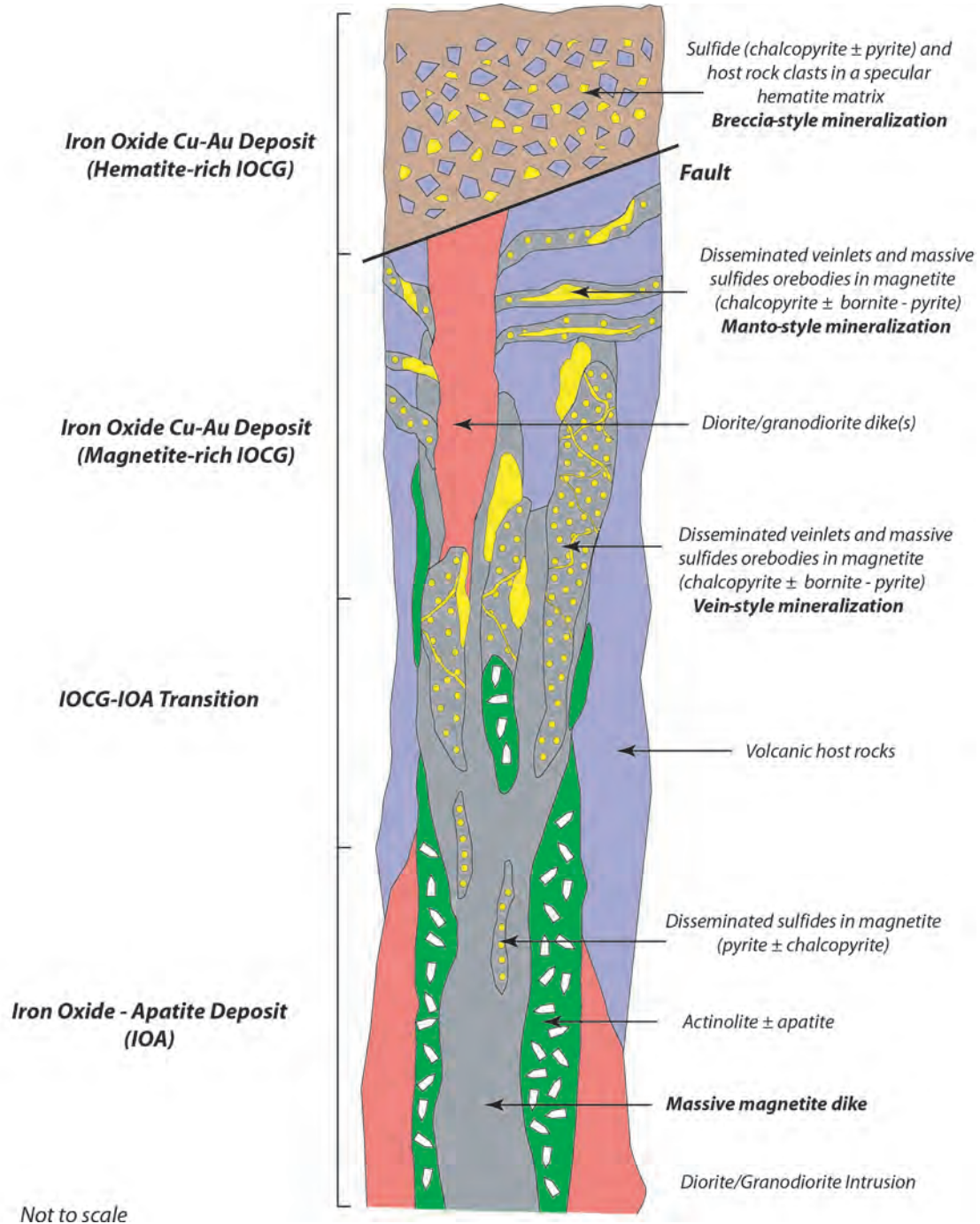


Fig. 2. Vertical transition from Kiruna-type IOA mineralization at depth toward magnetite-rich IOCG mineralization at intermediate levels, and hematite-rich IOCG mineralization at the shallowest levels of the system. The schematic cross section is based on observations of deposits throughout the Chilean iron belt. Host rocks for IOCG and IOA deposits range from felsic to mafic igneous rocks, clastic to chemical sedimentary rocks, and their metamorphic equivalents. Modified from Barra et al. (2017).

into the Si-rich melt and not the conjugate Fe-rich melt ($D_{H_2O}^{Si-liq/Fe-liq} = 1.4 - 2.5$; Hou et al., 2018). This finding disallows the possibility that an immiscible, dense, H_2O -poor, Fe-P-O-rich melt could ascend from its conjugate, less dense, H_2O -, Si-rich melt, or evolve a hydrothermal fluid capable of forming an IOCG deposit. Further, we highlight that the liquid immiscibility experiments of Hou et al. (2018) produced

an immiscible Fe-P-O melt that contains nearly 40 wt % P_2O_5 . This is an order of magnitude more phosphorus than is present in Kiruna-type IOA deposits. The Fe-P melts are also enriched in Ti relative to the Si-rich conjugate melt, with values of $D_{Ti}^{(Fe-liq)/(Si-liq)}$ of 2 to 2.5. Thus, magnetite that crystallizes from the Fe-P melt should be Ti rich, which is opposite to what is reported for Kiruna-type IOA deposits.

Experimental data that constrain the partitioning of oxygen isotopes between immiscible Fe- and Si-rich melts also disallow the liquid immiscibility model to explain Kiruna-type IOA deposits. Lester et al. (2013b) experimentally constrained oxygen isotope partitioning between immiscible Fe- and Si-rich melts, and report that $\Delta^{18}\text{O}$, which is defined as $\delta^{18}\text{O}_{\text{Si-rich melt}} - \delta^{18}\text{O}_{\text{Fe-rich melt}}$, is roughly between 0.0 and 0.5‰ at 1,100° to 1,200°C. Thus, for example, if the parent melt that unmixes to produce Fe- and Si-rich conjugate melts is an andesite, as proposed for El Laco (Tornos et al., 2016), the Fe-rich melt should have a $\delta^{18}\text{O}$ value of ~6.5 to 8.5‰, using the $\Delta^{18}\text{O}$ value of 0.5‰ from Lester et al. (2013b). Similarly, using the $\Delta^{18}\text{O}$ value of 0.0‰ from Lester et al. (2013b) requires that the El Laco orebodies have a $\delta^{18}\text{O}$ value of ~7 to 9‰. However, $\delta^{18}\text{O}$ values of 3.5 to 5.5‰ are reported for magnetite from El Laco (Tornos et al., 2016), and are not consistent with liquid immiscibility. Rather, these measured $\delta^{18}\text{O}$ values are consistent with magnetite that crystallizes directly from an intermediate silicate melt or a magmatic-hydrothermal fluid (cf. Taylor, 1967, 1968). It is relevant to note that no study has yet reported conclusive analytical evidence in natural samples that supports the liquid immiscibility hypothesis as a genetic mechanism that explains the formation of Kiruna-type deposits. In fact, recent studies in the Kiruna district in Sweden favor a model that involves magmatic-hydrothermal fluids in the genesis of the Fe ores (Westhues et al., 2016, 2017a). In short, the hydrothermal nature of the ore zircon grains at Kiruna and the isotopic signatures point to a hydrothermal influence on the Fe ore formation, with a high-temperature magmatic fluid related by the intrusions as the most likely heat and fluid source (Westhues et al., 2017b).

Recently, Knipping et al. (2015a) proposed a novel geologic model that invokes a synergistic combination of purely igneous and magmatic-hydrothermal processes to explain the formation of Kiruna-type and IOCG deposits as part of the same evolving system. The model was developed after intensive study of the field relationships, trace element geochemistry, and Fe and O stable isotope composition of magnetite from the Los Colorados magnetite-apatite deposit, one of the largest and least altered Kiruna-type deposits in the Chilean iron belt. Briefly, the model proposes that magnetite microlites (i.e., magnetite grains of 10- to 100- μm range) crystallize from silicate melts of intermediate to mafic silicate composition, followed by decompression-induced volatile saturation of the melt wherein the bubbles of magmatic-hydrothermal fluid nucleate and grow on the crystal faces of magnetite microlites. The magnetite microlites and magmatic-hydrothermal fluid form a magnetite-fluid suspension within the magma chamber wherein the magnetite microlites are encapsulated within the fluid. The suspension has a bulk density less than the surrounding magma, allowing the suspension to ascend through the magma chamber (in essence, the process is analogous to sulfide flotation during physical beneficiation of sulfide ore). In addition, Fe is highly soluble in magmatic-hydrothermal fluids, and the magnetite microlites in the suspension will continue to grow during ascent as they source Fe from the surrounding fluid, owing to the decrease of Fe solubility during decompression. Regional extension allows the magmatic-hydrothermal fluid-magnetite suspension to evolve from the magma via preexisting, structurally enhanced dilatant zones that act as conduits (e.g., faults, fractures zones,

brecciated host rocks, volcanic feeder zones, caldera systems, etc.). The resulting fast ascent of the suspension implicates sudden decompression and cooling that will lead to the precipitation of hydrothermal magnetite surrounding the previously formed igneous magnetite microlites, or forming veins, disseminations, or massive patches of hydrothermal magnetite that do not form around igneous cores. Simultaneously, the ore fluid will continue to ascend and transport remaining dissolved Fe as well as dissolved Cu, Au, S, and other elements that partition strongly from silicate melt into magmatic-hydrothermal fluid. As the fluid further cools and becomes oxidized at shallow paleodepths, Fe oxides (i.e., magnetite, hematite), and Fe-Cu-Au-bearing sulfides (i.e., chalcopyrite, bornite, pyrite) will precipitate from the fluid to form IOCG deposits.

Since publication of this novel igneous/magmatic-hydrothermal flotation model, our research group has continued to investigate samples from Los Colorados, performing high-resolution analyses of magnetite, apatite, actinolite, and pyrite. The data set includes whole-rock geochemistry; minor and trace element compositions of magnetite; O, H, and Fe stable isotope abundances in magnetite; trace element chemistry of late-stage pyrite and magnetite; O and H stable isotope abundances of actinolite; characterization of micro- to nanoscale inclusions in late-stage hydrothermal magnetite; and Re-Os isotope systematics of magnetite and pyrite. All these data are consistent with the flotation model proposed by Knipping et al. (2015a). We also investigated samples from other similar Kiruna-type IOA deposits in the Chilean iron belt, including the Carmen, El Romeral, and Cerro Negro Norte, and Mantoverde, Candelaria, Barreal Seco, Diego de Almagro, and Casualidad IOCG deposits. These studies are being complemented with data from the younger, Plio-Pleistocene El Laco IOA deposit in the Chilean Altiplano, and the much older Precambrian Pea Ridge and Pilot Knob IOA deposits in Missouri, United States. The data from these deposits are also consistent with a combined igneous/magmatic-hydrothermal model, in agreement with recent studies of deposits in the Kiruna district in Sweden (Jonsson et al., 2013; Weis, 2013; Westhues et al., 2016, 2017a, b). In particular, our recent paper that focuses on the world-class El Romeral deposit in the Chilean iron belt provides the first geochronological evidence linking IOA mineralization (Cerro Principal Fe orebody) with the intrusion of the Romeral Diorite (Rojas et al., 2018).

In this paper, we review and clarify our recently proposed model that invokes a synergistic combination of igneous and magmatic-hydrothermal processes to explain the formation of Kiruna-type deposits and their observed spatial and temporal association with IOCG deposits. The results indicate that the model is geologically plausible for IOA and/or IOCG deposits formed in arc settings, where there is abundant evidence that magnetite segregation is common in arc magmas (Edmonds et al., 2014), although most of the time the optimal conditions for massive accumulation are not met, unlike ore systems. Hence, a key focus of our studies is set on identifying the geologic factors leading to the efficient accumulation of igneous magnetite to form an ore deposit in magmatic settings. The fundamental geochemical processes outlined here inform discussions for IOA and IOCG systems formed in nonarc environments. It is important to note that the model does not explain all observations at all deposits. The model

is flexible, and can accommodate geologic variability of the premineralized crustal architecture within and among mineralized districts, as well as the composition of the subarc mantle that is the ultimate source of magmas that pond in the upper crust and from which the magnetite-fluid suspension evolves. Thus, we suggest that the model is globally applicable when considering these geologic differences across space and time. Notably, we do not attempt to duplicate the many excellent comprehensive papers that review these deposit types (e.g., Sillitoe, 2003; Williams et al., 2005; Groves, 2010; Barton, 2014). We intend not to repeat, but to add to those reviews.

Geologic Setting

The Chilean iron belt is approximately 25 km wide and extends approximately 600 km north-south between latitudes 25° and 31° S in the Coastal Cordillera of northern Chile (Fig. 1). The belt contains Kiruna-type IOA, IOCG, and stratabound Cu(-Ag) deposits, which are commonly referred to as Manto-type Cu(-Ag) deposits (Fig. 1; Barra et al., 2017). Mineralization occurred during the Cretaceous, with ages that range from about 130 to 90 Ma (Oyarzún et al., 2003; Barra et al., 2017). The ore deposits in the belt are spatially associated with the Atacama fault system, a nearly 1,000-km-long, N-S-trending, trench-parallel system that resulted from the synchronous opening of the South Atlantic Ocean basin and oblique subduction beneath western South America (Uyeda and Kanamori, 1979; Scheuber and Andriessen, 1990; Brown et al., 1993). The resulting transpressional regime created the crustal-scale, strike-slip Atacama fault system, which provided the structural pathways for the ascent of mantle-derived magmas that formed the volcanic and plutonic rocks that serve as the predominant hosts for mineralization. Those same structural pathways subsequently acted as the pathways for hypogene ore fluid(s) during regional extension.

The Los Colorados IOA deposit is located at 28°18'18" S and 70°48'28" W, about 35 km north of Vallenar, Chile. Measured resources are 873 million metric tons (Mt) at an average grade of 34.6% Fe, with proven reserves of ~446.1 Mt at a grade of 36.5% Fe as of March, 2015 (CAP summary, 2016). The deposit formed at ~110 Ma and is hosted in andesitic to basaltic andesitic volcanic and volcanoclastic rocks of the Punta del Cobre Formation (Pichon, 1981; Oyarzún and Frutos, 1984; Pincheira et al., 1990). Mine geologists estimate that the ore deposit formed 3 to 4 km beneath the paleosurface (CAP, pers. commun.). The deposit consists of two high-grade, massive tabular orebodies, as well as mineralized breccia bodies, and disseminated and veinlet mineralization (Fig. 3). The two tabular orebodies are referred to by mine geologists as the Western and Eastern dikes. The Western dike is dominated modally by massive magnetite (≥ 90 vol %), with minor amounts of actinolite, pyrite, and apatite. The Western dike strikes N10°–15° E to N-S, is approximately 1,500 m long, 500 m deep, and varies in width from 90 to 180 m. The orebody is hosted within the district-scale Los Colorados fault, which is part of the Atacama fault system, and was the structural control for ore fluid(s) (Knipping et al., 2015a; Reich et al., 2016). The Eastern dike is a smaller, tabular orebody composed of massive magnetite (≥ 85 vol %) with minor amounts of actinolite, apatite, and pyrite. This orebody measures about 780 m long, is about 500 m deep, 50 m wide, and the strike

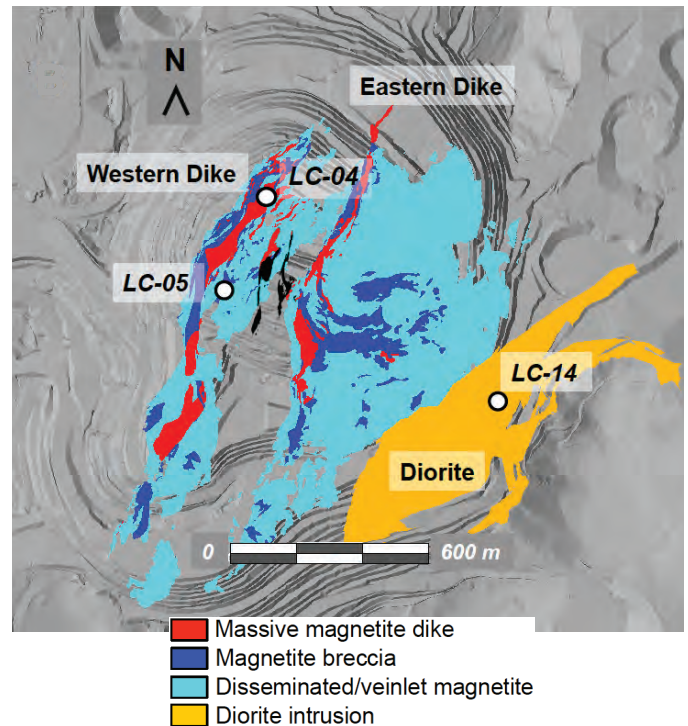


Fig. 3. Mineralization at the Los Colorados Kiruna-type IOA deposit is shown in plan view along with locations of drill cores in the main magnetite orebody (LC-04 and LC-05) and the diorite intrusion (LC-14). Topography of the mine is used as background for the mapped ore distribution. Modified from Reich et al. (2016).

changes from N10°–15° W to N10°–15° E from the central to the northern portions of the orebody.

The Western and Eastern dikes each grade outward from massive magnetite to intergrowths of magnetite and large actinolite crystals, to disseminated mineralization in the volcanic and/or diorite host rocks. Disseminated mineralization, which consists of up to 5 vol % each of disseminated magnetite and pyrite, and minor amounts of chalcopyrite, extends for hundreds of meters to the east of the Eastern dike into a diorite intrusion (Fig. 3). Veinlets comprised of actinolite, magnetite, and pyrite crosscut the diorite intrusion, as well as the Western and Eastern dikes.

Samples for this study were collected from drill cores LC-04 and LC-05, which penetrate the northern and central parts of the Western dike, respectively, and LC-14 that penetrates the diorite intrusion (Fig. 3). Drill core LC-04 is collared at 196 m and penetrates 146 m into the orebody. Drill core LC-05 is collared at 345 m and penetrates 150 m into the orebody. Drill core LC-14 is collared at 509 m and penetrates 173 m into the brecciated diorite. Drill cores LC-04 and LC-05 sample massive magnetite, as well as disseminated pyrite and veinlets of actinolite, magnetite, and pyrite with the massive magnetite orebody. Samples from drill core LC-14 reveal disseminated grains of magnetite, pyrite, and actinolite, as well as veinlets consisting of all three minerals. Bulk-rock compositions were obtained for six samples from drill core LC-04, five samples from drill core LC-05, and four samples from drill core LC-14. Drill core samples were selected to cover the entire depth within each core.

Analytical Methods

Several analytical techniques were used to quantify the composition of whole-rock samples and individual minerals. Each technique is described in detail in other publications and only a summary of each is presented here with the primary resource(s) for those data. Briefly, inductively coupled plasma-optical emission spectroscopy (ICP-OES) and inductively coupled plasma-mass spectrometry (ICP-MS) were used to quantify the abundances of major elements and trace elements, respectively, in whole-rock samples (Knipping et al., 2015b). Electron probe microanalysis (EPMA) was used to quantify the abundances of Mg, Al, Si, Ca, Ti, V, Mn, and Fe in magnetite grains (Knipping et al., 2015a, b; Deditius et al., 2018); Fe, Mg, Ti, Al, Si, K, Ca, Mn, Na in actinolite (Bilenker et al., 2016); the abundances of Fe, Au, Te, Cu, Ni, Zn, Co, S, Ag, Cd, Sb, Pb, As, and Se in pyrite (Reich et al., 2016). EPMA was also used to generate wavelength-dispersive spectrometry (WDS) X-ray maps for major and trace elements in both magnetite and pyrite. Laser ablation ICP-MS (LA-ICP-MS) was used to measure the abundances of Fe and 38 trace elements along transects in magnetite grains (Knipping et al., 2015b). The LA-ICP-MS transects were performed on magnetite grains along the same profiles that were previously analyzed with EPMA. The abundances of stable ^{18}O and ^{16}O in magnetite and actinolite separates were measured by using a laser fluorination line attached to a gas isotope ratio mass spectrometer in dual inlet mode, and using BrF_5 as reagent (Bilenker et al., 2016). The abundances of stable ^{56}Fe and ^{54}Fe in magnetite separates were measured by using a Nu Plasma HR multi-collector ICP-MS in dry plasma mode (Bilenker et al., 2016).

The abundances of stable ^1H and ^2H in magnetite and actinolite separates were measured by using a thermal conversion elemental analyzer with a MAT253 gas source isotope ratio mass spectrometer (Bilenker et al., 2016). Secondary ion mass spectrometry (SIMS) was used to measure the abundances of Cu, As, Se, Ag, Sb, Te, and Au in pyrite (Reich et al., 2016). Negative-thermal ionization mass spectrometry (N-TIMS) was used to measure the abundances of ^{187}Re , ^{187}Os , and ^{188}Os in magnetite and pyrite mineral separates (Barra et al., 2017). Transmission electron microscopy (TEM) and scanning transmission electron microscopy (STEM) were used to analyze nano- and micron-scale inclusions in late-stage hydrothermal, disseminated magnetite grains (Deditius et al., 2018).

Results

Whole-rock compositions

A detailed table of major, minor, and trace elements compositions (total of 70 elements) of the bulk-rock samples is reported in Knipping et al. (2015b). The Fe content of the massive, tabular orebodies varies significantly with depth from up to 99 to 52 % Fe_2O_3 . However, drill core LC-04 also includes a sharp contact between the massive Western dike and a crosscutting diorite dike, with a sudden change from ~73 to 6 wt % Fe_2O_3 within 4 m (LC-04-125.3 vs. LC-04-129.5). The REE concentrations of the bulk rock of the diorite intrusion and the magnetite dikes are illustrated in Figure 4. The massive magnetite ore from the Western (magnetite) dike and the brecciated diorite intrusion have similar REE patterns, including a pronounced negative Eu anomaly and a horizontal heavy REE distribution. However, the brecciated

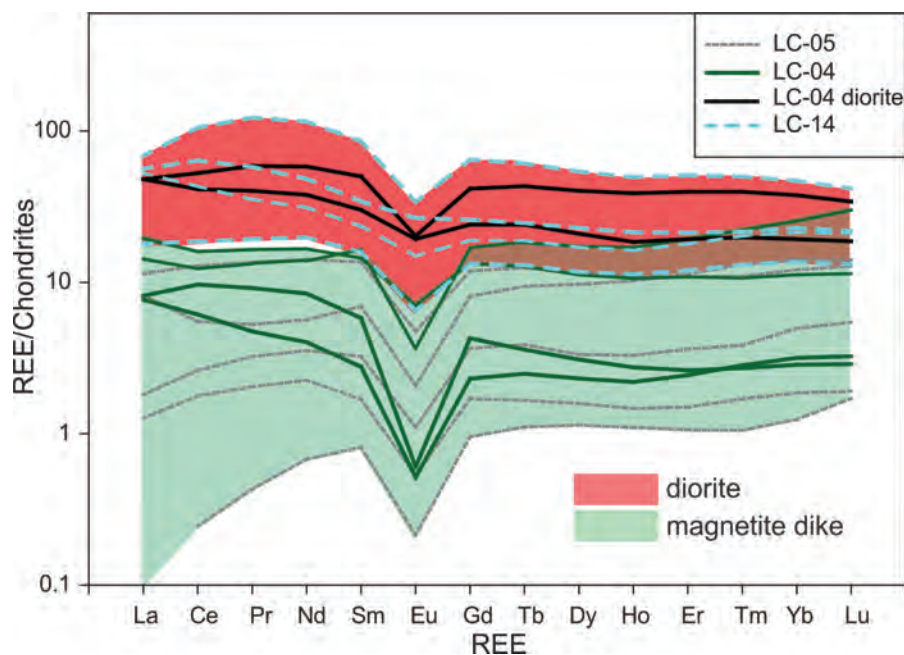


Fig. 4. Rare earth element (REE) concentrations in the bulk-rock samples of the magnetite dike (gray) and the diorite intrusion (blue) normalized to chondrite (Sun and McDonough, 1989). The diorite intrusion has distinctly higher REE concentrations, but shows in general a similar REE pattern (negative Eu anomaly, horizontal HREE distribution), when compared to the magnetite dike. Note that all samples from drill core LC-05, and all except two samples from drill core LC-04, intersect the massive magnetite western orebody. The two samples from drill core LC-04 that plot at higher values of REE/chondrites were collected from the bottom of the drill hole where it intersects diorite host rock proximal to the main massive magnetite orebody. Modified from Knipping et al. (2015b).

diorite intrusion has distinctly higher REE concentrations than the magnetite dikes. Also, decreasing Fe content is correlated with increasing light REE.

Magnetite textures

Magnetite in the Western dike: Examination of magnetite grains by using backscattered electron (BSE) imaging reveals multiple textural types of magnetite. Among samples from the massive, tabular Western dike, some magnetite grains appear optically pure, i.e., devoid of inclusions, some grains contain inclusion-rich cores and -free rims, some grains exhibit oscillatory zoning, and some grains contain crystallographically controlled exsolution lamellae (Fig. 5). A majority of the magnetite grains are characterized by having a subhedral to euhedral, inclusion-bearing core that is surrounded by an inclusion-free rim. The

cores have diameters that range from a few tens of microns to a few hundred microns (Fig. 6). The polycrystalline inclusions range in size from submicron to several tens of microns, and are randomly distributed within magnetite cores. The inclusions measuring $\geq 10 \mu\text{m}$ were identified by EDX analyses as actinolite or clinopyroxene, titanite, and an unspecified Mg-Al-Si phase. A polycrystalline inclusion that contains halite and titanite was identified in the most Fe rich sample (Fig. 7).

Disseminated and veinlet magnetite in the diorite intrusion: Among samples from drill core LC-14, which samples late-stage, disseminated, and veinlets of hydrothermal magnetite, magnetite grains are texturally more diverse than magnetite grains from the Western dike. Magnetite grains from drill core LC-14 are characterized by three different textures referred to as magnetite-X, -Y, and -Z (Fig. 8; Deditius et al.,

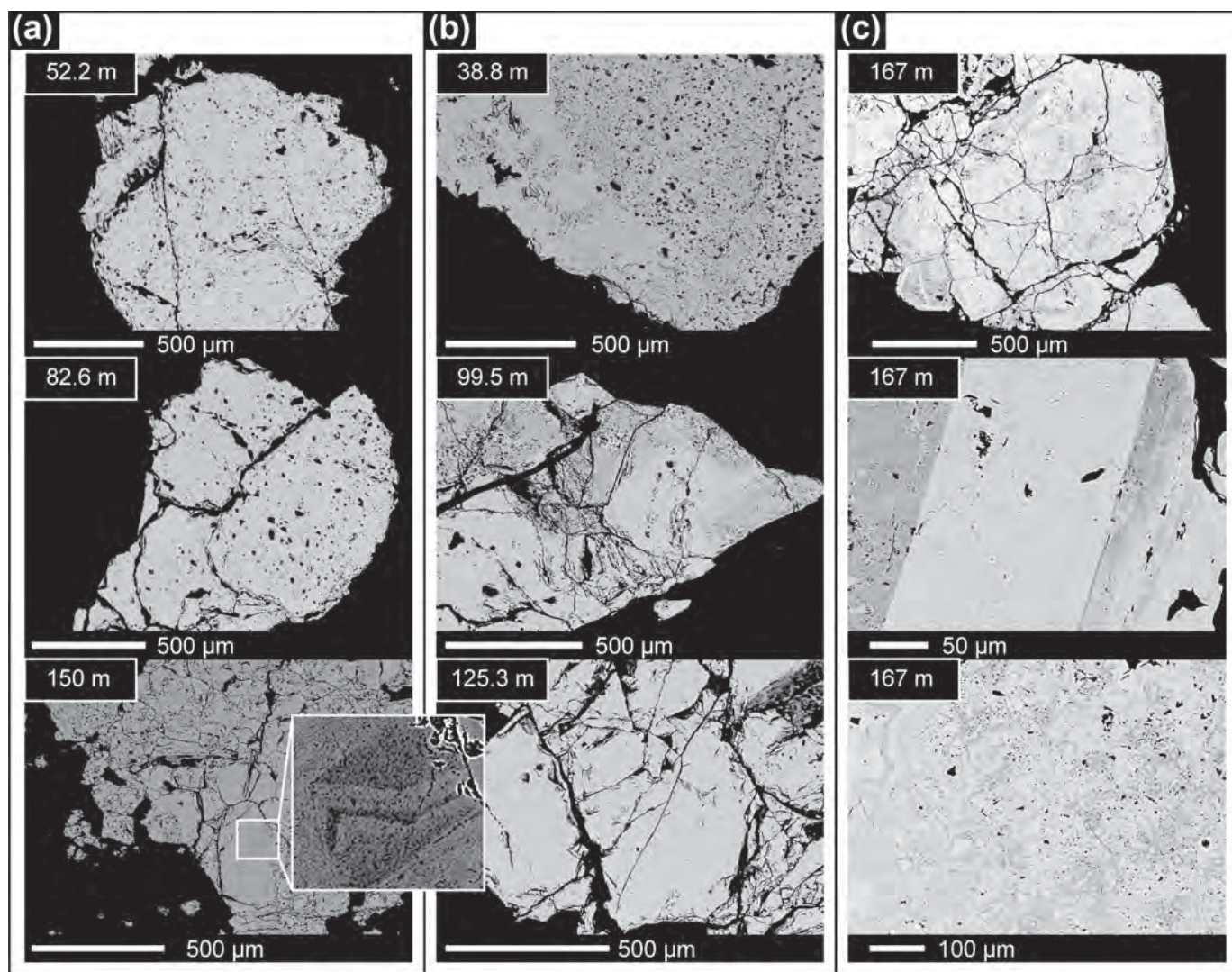


Fig. 5. Backscattered electron images of different magnetite grains from drill core LC-05 (column a), LC-04 (column b), and LC-14 (column c). (a). Randomly distributed inclusions in relatively pristine magnetite (depth 52.2 and 82.6 m) and inclusion-rich areas and inclusion-poor areas with some zoning (depth 150 m). (b). Pristine magnetite and inclusion-rich areas with small fine distributed inclusions to large randomly distributed irregular inclusions (depth 38.8 m), magnetite with different gray shades, indicating different trace element concentration (depth 99.5 m) and pristine magnetite (depth 125.3 m). (c). Oscillatory zoned magnetite with different gray shades (depth 167 m), magnetite with crystallographically oriented spinel exsolution lamellae in bright area and as small inclusions in dark gray areas (depth 167 m) and oscillatory zoning of bright and dark gray magnetite (depth 167 m). From Knipping et al. (2015b).

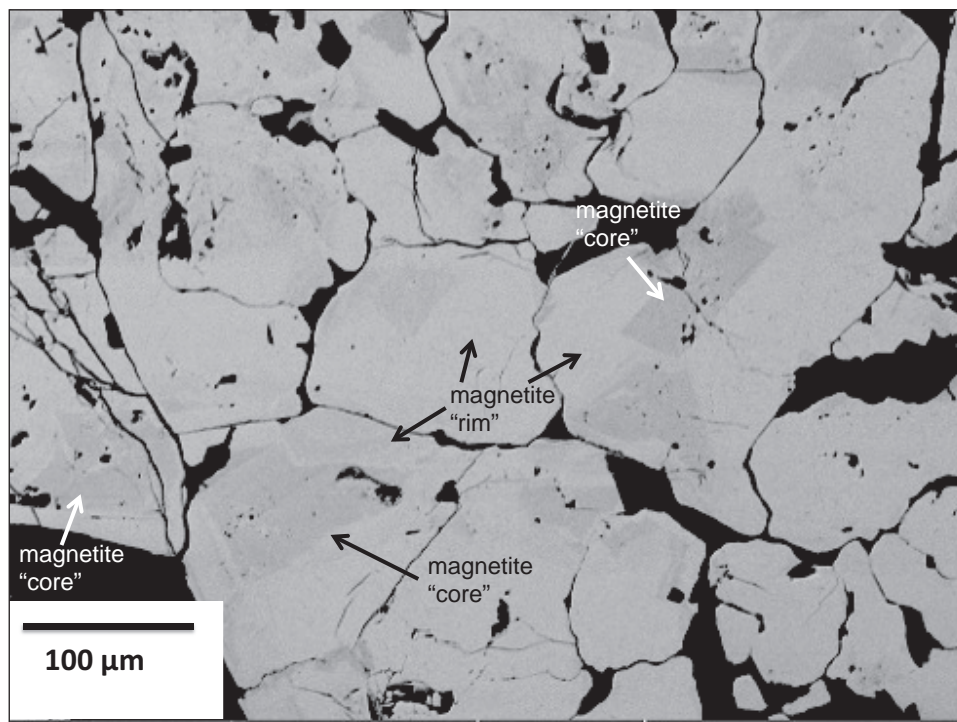


Fig. 6. Backscattered electron images of different magnetite grains, showing areas denoted by the authors as “cores” and “rims.” The darker gray areas, the cores, contain higher concentrations of the trace elements Ti, Mn, Al, relative to the lighter gray areas. The magnetite cores ubiquitously contain inclusions, whereas the rims are generally devoid of inclusions.

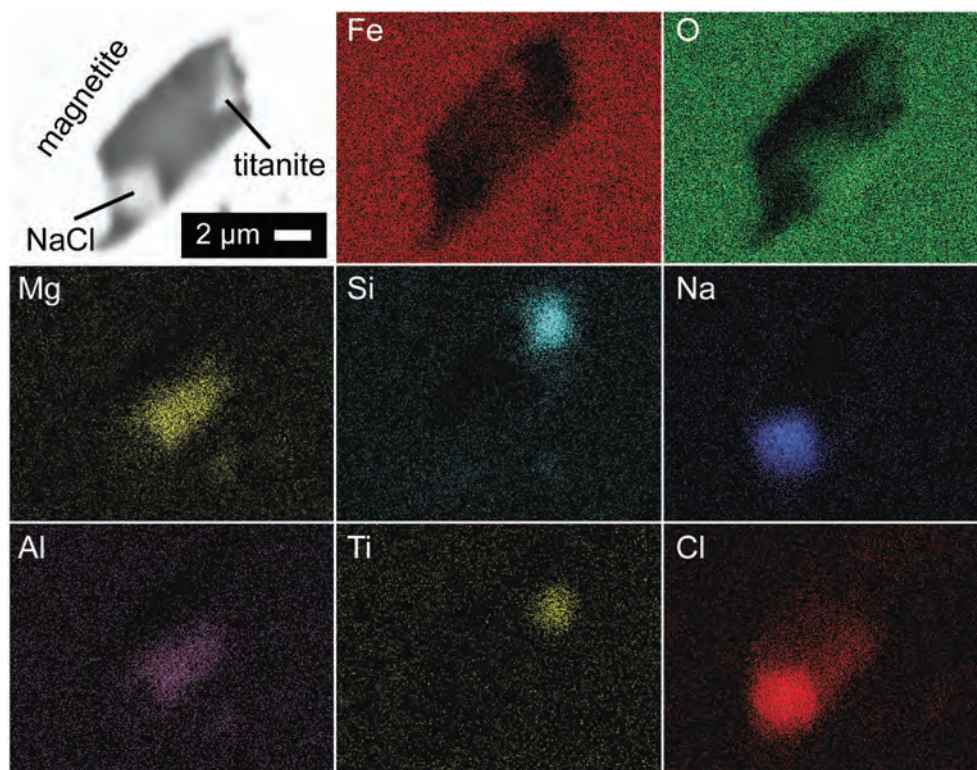


Fig. 7. Example of an energy dispersive X-ray spectroscopy elemental map of a small magnetite-hosted fluid inclusion ($<5 \mu\text{m}$) trapped in the massive magnetite of the most Fe rich bulk sample, from drill core LC-05 (sample LC-05-106 in Knipping et al., 2015b). The inclusion is heterogeneous with distinct titanite and halite crystals, implying a saline environment during magnetite crystallization. From Knipping et al. (2015b).

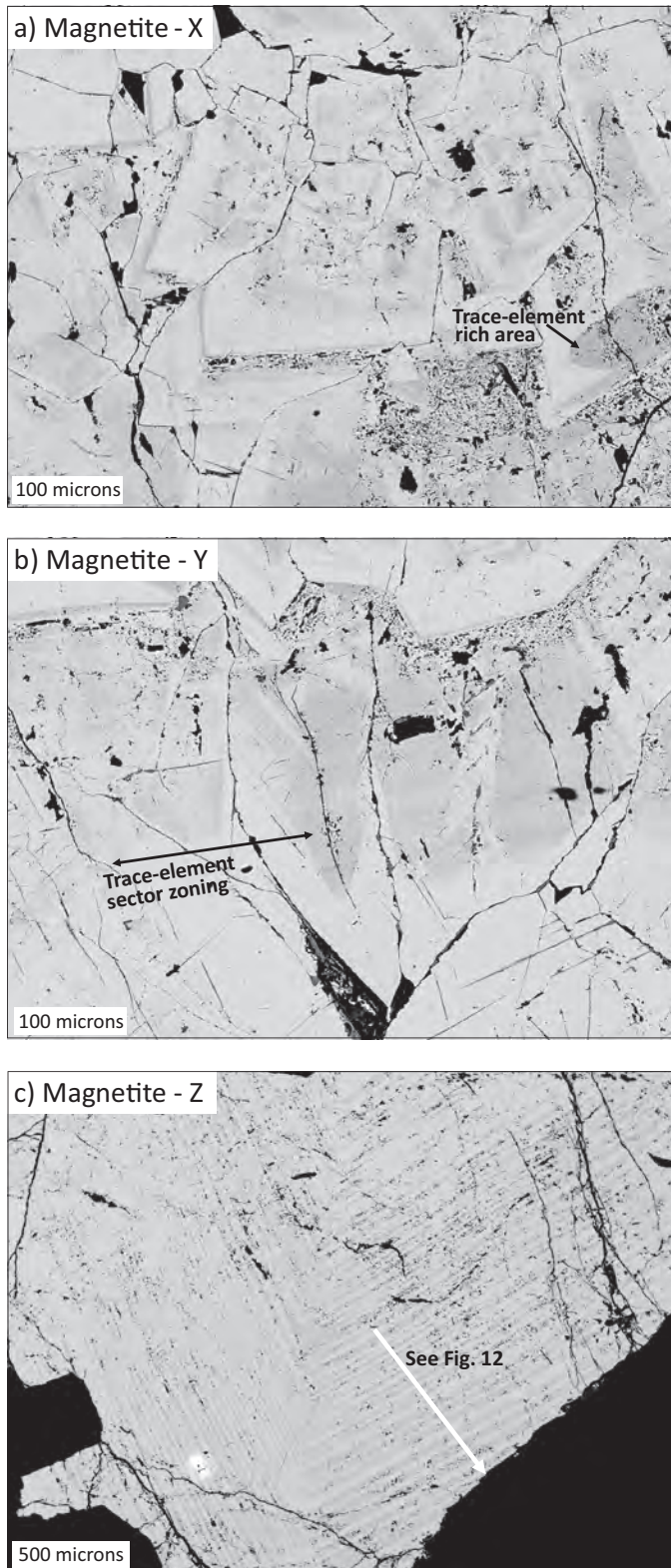


Fig. 8. Backscattered electron images of zoned, late-stage, hydrothermal magnetite from drill core LC-14. Magnetite-X, -Y, and -Z are shown as panels (a), (b), and (c). Darker gray corresponds to trace element-rich zones, and lighter gray to white corresponds to trace element-poor zones. A representative electron microprobe traverse along transect T1 in (c) is presented in Figure 12 along with semiquantitative trace element composition maps. Modified from Deditius et al. (2018).

2018). Magnetite-X is characterized by oscillatory and sector zoning of euhedral grains (Fig. 8a). Darker shades of gray visible in BSE images indicate trace element enrichment relative to lighter shades of gray. Grains of magnetite-X are partly recrystallized to fine-grained microcrystalline aggregates of magnetite and silicates, and preserve evidence for dissolution-reprecipitation processes. Magnetite-Y is characterized by a tooth-like texture with grain sizes on the order of $500\ \mu\text{m}$ (Fig. 8b). Magnetite-Z, modally the most abundant of the three types of hydrothermal magnetite in the brecciated and mineralized diorite, is characterized by oscillatory zoning with individual bands ranging in diameter from 2 to $10\ \mu\text{m}$ (Fig. 8c).

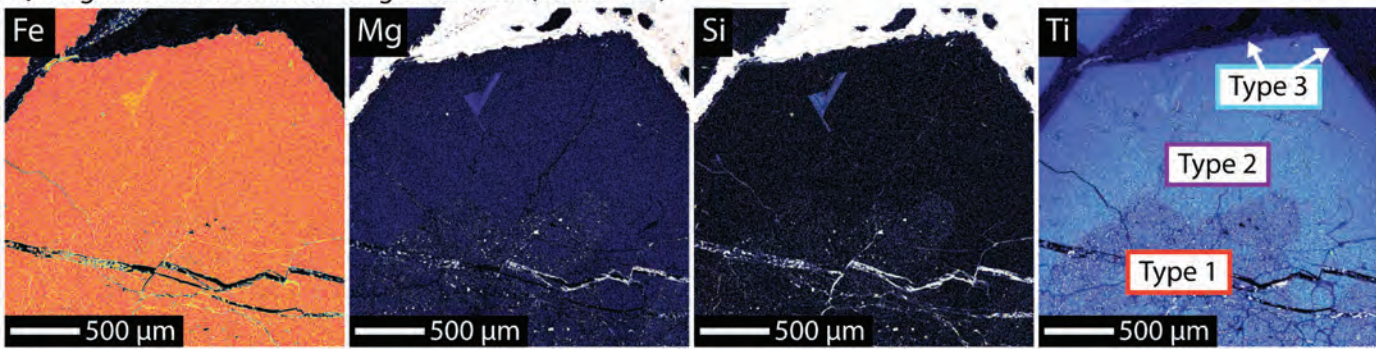
Magnetite chemistry

Magnetite in the main orebody: Individual magnetite grains among all samples exhibit significant trace element variability. In magnetite grains from the Western dike, EPMA and LA-ICP-MS analyses reveal that the concentrations of some trace elements, e.g., Ti, Al, and Mn, are ubiquitously enriched in the magnetite cores relative to the rims. The concentrations of trace elements are highest in the cores and decrease systematically from core to rim (Fig. 9). EPMA WDS X-ray element maps reveal that the concentration of Fe is homogeneous within magnetite grains, whereas the WDS X-ray maps reveal enrichment of Ti, Mg, and Si in the magnetite core (Fig. 9). In the case of Ti, the X-ray maps reveal distinct Ti depletion from the core to rim of individual grains, with three different zones (Fig. 9a), including Ti- and inclusion-rich cores, Ti-poorer and more pristine transition zones, and Ti-depleted rims. These three compositionally distinct zones of magnetite grains are referred to as type 1, type 2, and type 3 magnetite, as originally defined by Knipping et al. (2015a).

The EPMA data reveal a systematic decrease in the concentrations of Ti, Al, and Mn, where magnetite type 1 contains the highest concentration of these trace elements, and their concentration systematically decreases from type 1 to type 2 to type 3 (Fig. 10). The type 1 compositions plot in the igneous box in the discriminant diagram, consistent with magnetite from Fe-Ti/V deposits and igneous rocks. Type 2 compositions plot within the porphyry box, consistent with magnetite that crystallized from moderate- to high-temperature magmatic-hydrothermal fluid. Type 3 magnetite plots in the field for Kiruna-type deposits. We highlight that the variability shown in Figure 10 for $[\text{Ti} + \text{V}]$ reflects dominantly variability in the concentration of Ti. Most of the analyzed magnetite grains from the massive magnetite Western dike show no significant variation in V within individual grains (variations per measured profile are $<0.01\ \text{wt}\%$). However, the V content of magnetite varies with depth and distance to the dike; i.e., V decreases upward and distal from the dike center. We note that regardless of potential concerns regarding the use of discriminant diagrams to classify ores, our magnetite data show a distinctive trend from high-temperature, igneous-like signatures that progressively grade toward lower temperature, hydrothermal compositions in the magnetite rims (types 1, 2, and 3, Fig. 10).

The LA-ICP-MS data provide complementary information about trace elements that were below detection limit using EPMA, and are of particular importance to investigate iron ore deposits (e.g., Cr, Ni, Co, Ga, Zn, Sn). The low detection limits

a) magnetite from massive magnetite dike (LC-05-129)



b) magnetite from diorite intrusion (LC-14-167)

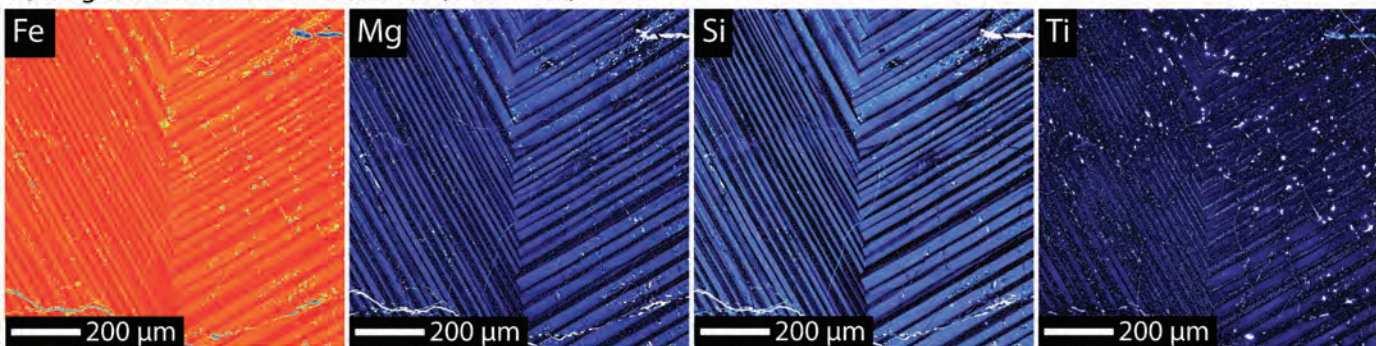


Fig. 9. A representative wavelength dispersive X-ray elemental map of selected trace elements in magnetite from Los Colorados. (a). Magnetite sample from drill core LC-05 that penetrates the massive orebody (sample LC-05-129 in Knipping et al., 2015b) that contains a Ti- and inclusion-rich grain core (type 1), which is surrounded by inclusion-poor magnetite that contains less Ti (type 2) and a Ti-depleted rim (type 3). (b). Magnetite from drill core LC-14 that penetrates the brecciated diorite intrusion (sample LC-14-167 in Knipping et al., 2015b) that exhibits oscillatory zoning, typical of crystal growth from a compositionally fluctuating fluid.

as well as the continuous detection signal by LA-ICP-MS allows for a better visualization of zoned grains when compared with BSE images and point measurements by EPMA, respectively. While the concentration of V in the massive magnetite ore seems to remain constantly high across each measured grain, as already observed in the majority of the EPMA profiles, the concentration of Cr remains consistently low and is often below

detection limit. High V (>500 ppm) and low Cr concentration (<100 ppm) in magnetite have been reported for many other Kiruna-type deposits (Loberg and Horndahl, 1983; Nyström and Henriques, 1994; Core, 2004; Dupuis and Beaudoin, 2011; Dare et al. 2014, 2015), and Knipping et al. (2015b) proposed plotting V versus Cr as a new discrimination method to identify Kiruna-type deposits from IOCG, porphyry, and Fe/Ti-V

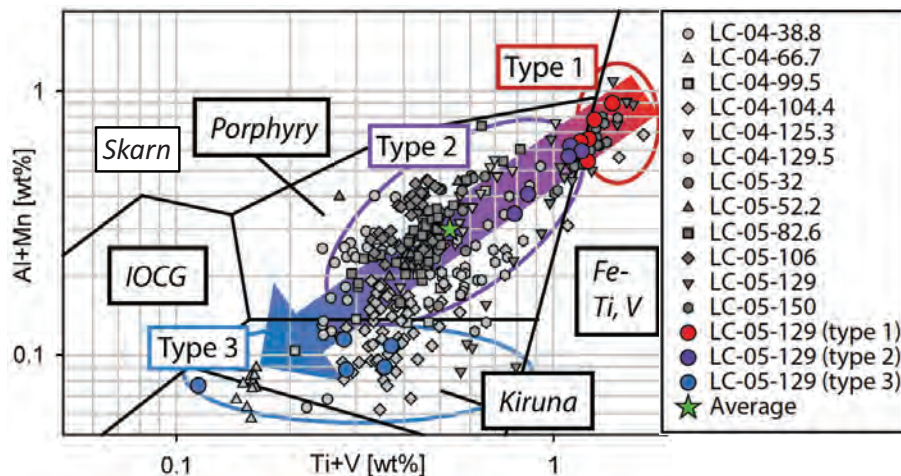


Fig. 10. The concentrations of Ti, V, Al, and Mn are plotted in the magnetite discriminant diagram from Nadoll et al. (2014). The plot shows that the concentration of trace elements decreases systematically from type 1 to type 2 to type 3. The star is the average composition of all Los Colorados magnetite analyses.

deposits. The LA-ICP-MS data reveal that other important ore-discriminating elements in magnetite, such as Al, Ti, Mn, Ni, Ga, and Zn, are more enriched in magnetite cores when compared to rims, consistent with the concentrations for these elements reported from high-temperature magnetite in porphyry deposits and magnetite crystallized from silicate melt (Nadoll et al. 2014). For detailed tables with EPMA and LA-ICP-MS data, see Knipping et al. (2015a, b).

The LA-ICP-MS transects across magnetite grains also provide information about the mineral inclusions in the magnetite cores. Figure 11 shows a representative LA-ICP-MS transect across a single magnetite grain. This particular magnetite grain did not exhibit any visible zonation in BSE imaging. However, the LA-ICP-MS traverse reveals the presence in the magnetite core of inclusions that are enriched in Si, Al, Mn, and Mg, consistent with the element maps (Fig. 9), whereas LA-ICP-MS did not reveal inclusions in the magnetite rims. The concentrations of some trace elements, e.g., V, Ni, and Co, exhibit minimal variation across the entire magnetite grain, including core and rim, in contrast to the concentrations of, e.g., Ti, Sr, Hf, and Pb, which are enriched in the magnetite core and decrease abruptly at the core-rim boundary. This compositional zonation is ubiquitous among magnetite grains from the Western dike.

Disseminated and veinlet magnetite in the diorite intrusion:
The three types of hydrothermal, disseminated, and veinlet

magnetite hosted in the diorite intrusion, magnetite-X, -Y and -Z, are compositionally similar (Deditius et al., 2018). However, EPMA analyses and element mapping reveal that the trace element abundances vary systematically between the bands of oscillatory zoned magnetite grains in magnetite-Z (Figs. 9b, 12) varying from trace element-rich bands, which are dark gray in BSE images, to trace element-poor bands, which are light gray in BSE images (Fig. 12). The alternating trace element-rich and -poor bands range in thickness from 2 to 10 μm . Trace elements are enriched in sector zones of magnetite-Y. The magnitude of compositional variability between the trace element-rich and -poor bands is on the order of wt % for Si, Al, Ca, Mg, Ti, Mn, Na, and K. The EPMA analyses of late-stage, hydrothermal magnetite reveal systematically lower concentrations of Mg, Mn, Si, Al, Ti, and V than in magnetite from the Western dike (Fig. 13). The EPMA element maps of all three types of late-stage hydrothermal magnetite reveal also that the trace element-rich bands contain inclusions that are enriched in Si + Al (Fig. 9b). The X-ray elemental maps reveal the presence of inclusions enriched in Ti + Mn in the trace element-poor bands.

TEM analyses of late-stage, hydrothermal magnetite-Z reveal the presence of nano- to micron-sized particles. These analyses also reveal no structural distortion between the alternating trace element-rich and -poor bands. Thus, the compositional fluctuation manifested as oscillatory zoning

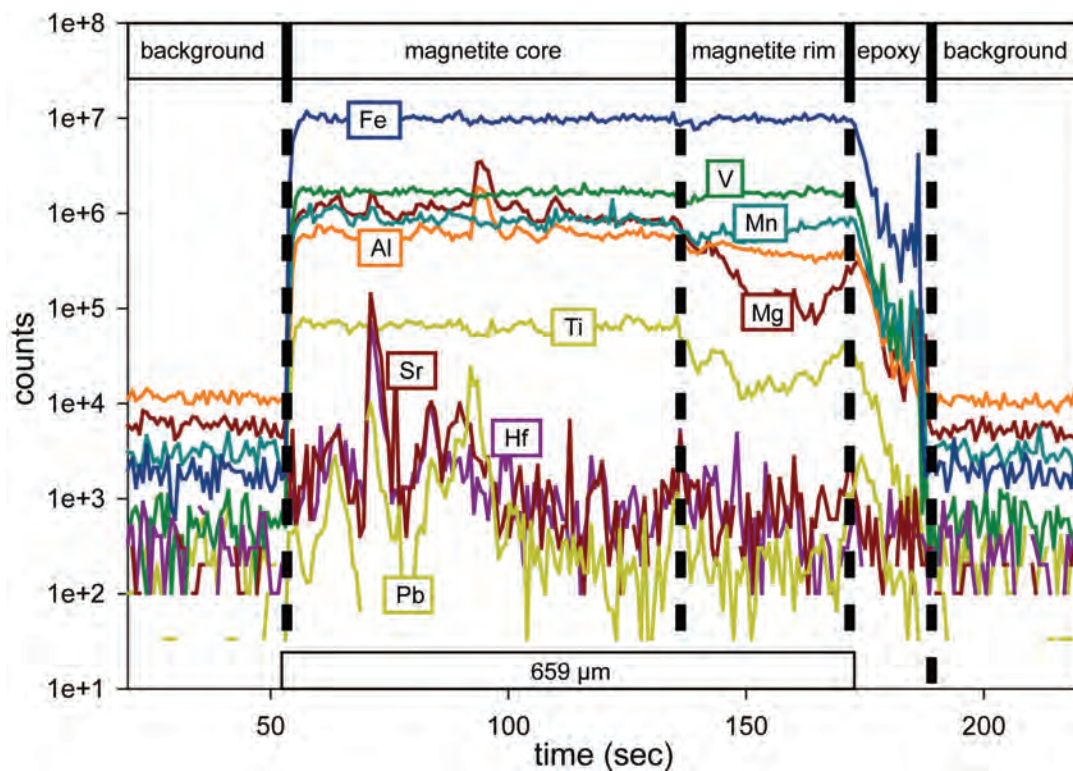


Fig. 11. A representative LA-ICP-MS analytical profile across a magnetite grain from drill core LC-05 that penetrates the massive magnetite orebody that did not show any visually resolvable zonation in BSE images (sample LC-05-82.6 in Knipping et al., 2015b). The LA-ICP-MS data reveal that particular elements such as Ti, Mg, Al, and Mn are enriched in the core and depleted in the rim of individual magnetite grains. Some elements, e.g., Mn, decrease in concentration at the core-rim boundary and then increase toward the outside of the grain. Some elements such as Sr, Hf, and Pb exhibit more variability but are clearly enriched in the magnetite core. Elements such as Co, Ni (not illustrated), and V show no variation from core to rim. Note that the X-axis indicates both time and distance; the sample was translated at a velocity of 5 $\mu\text{m/s}$ during the analysis, which results in a depth resolution of 3 to 6 μm for the transects. From Knipping et al. (2015b).

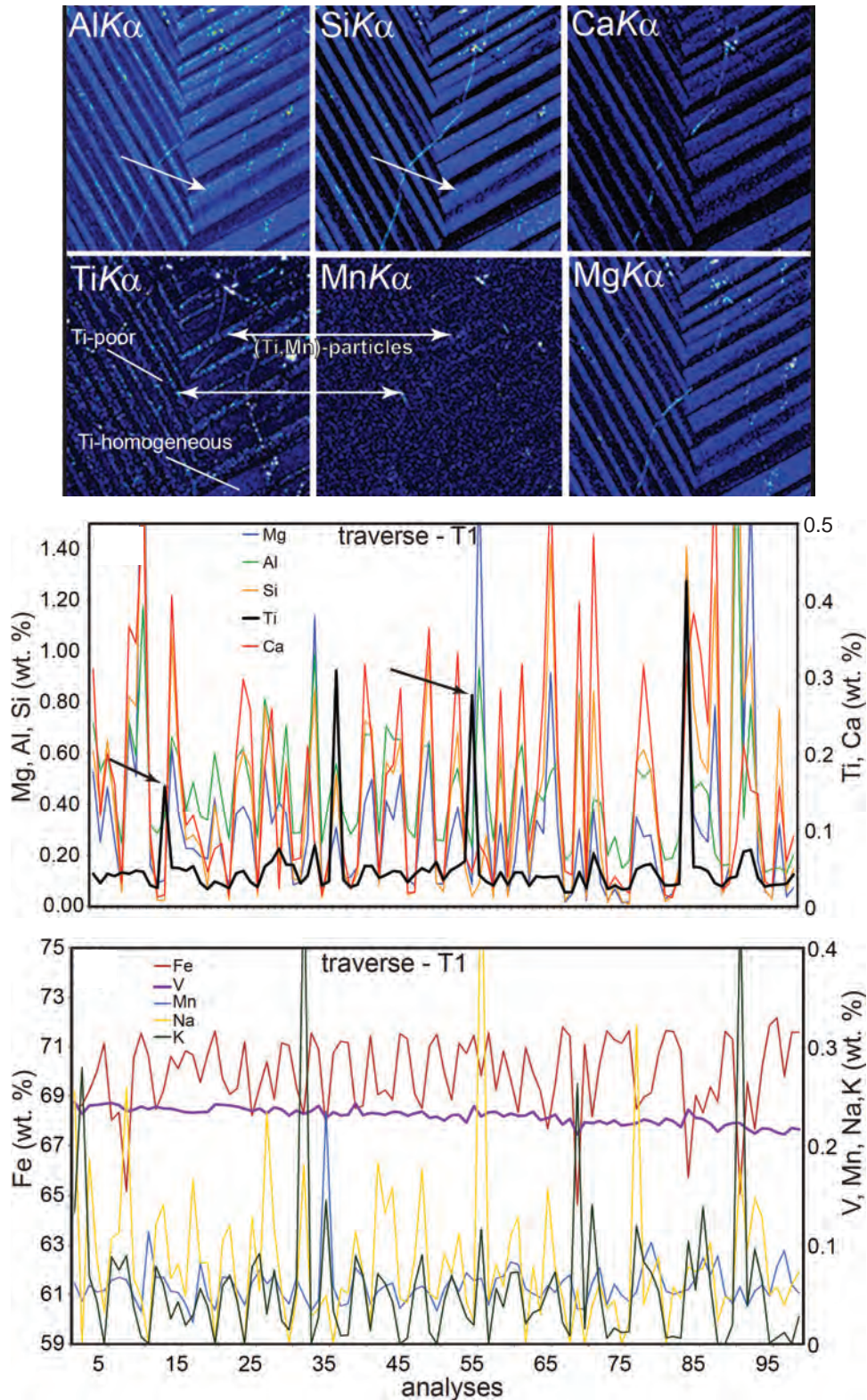


Fig. 12. A wavelength dispersive X-ray elemental map of Al, Si, Ca, Ti, Mn, and Mg in the area identified by the arrow in Figure 8c, and electron microprobe traverses along the area identified by the arrow in Figure 8c. See Figure 8c for scale bar. The elemental map reveals a similar distribution of Al, Si, Ca, and Mg between alternate trace elements-rich and -poor zones, the presence of (Si,Al) particles in trace element-rich zones (white arrows), distinct change of the concentration of Ti between particle-rich zones, homogeneously distributed Ti in Ti-rich zones, and Ti-poor zones, and a coherent correlation between Ti and Mn zones hosting particles. The bottom two panels reveal systematic changes in the concentration of Mg, Al, Si, Ti, Ca, Fe, V, Mn, Na, and K (in wt %) along traverse T1. Modified from Deditius et al. (2018).

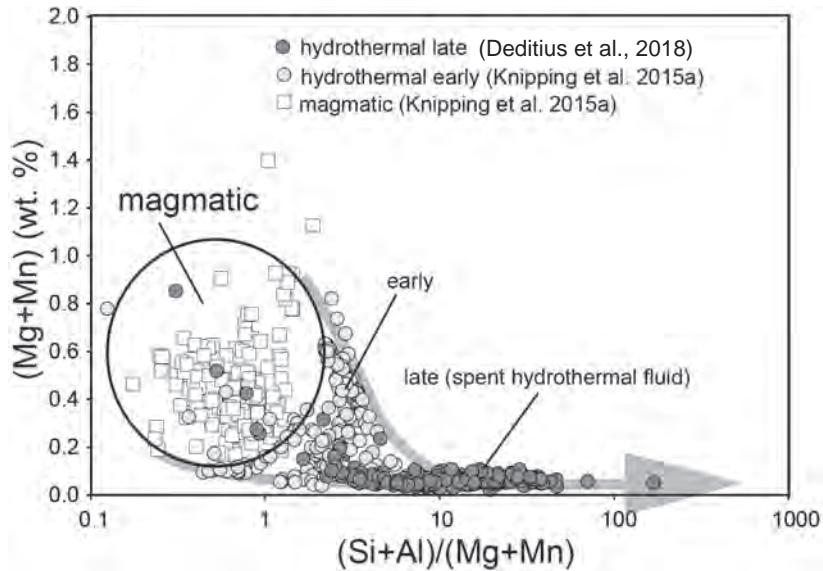


Fig. 13. The concentrations of [Mg + Mn] (in wt %) vs. [(Si + Al)/(Mg + Mn)] systematically decrease in magnetite from the main orebody (i.e., the Western dike) to late-stage, hydrothermal, oscillatory zoned magnetite in the brecciated diorite intrusion. Modified from Deditius et al. (2018).

is consistent with continuous growth of single crystals of magnetite from a hydrothermal fluid (Deditius et al., 2018). Six types of mineral nanoparticles were revealed by TEM techniques, including high-resolution imaging (HRTEM), selected area electron diffraction (SAED), high-angle annular dark-field scanning TEM (HAADF-STEM), and energy dispersive X-ray spectrometry (EDS): diopside, enstatite, amphibole (tremolite-actinolite), mica (phlogopite), and the (Fe-Ti) oxides ulvöspinel and Ti-rich magnetite. The nanoinclusions are hosted within single crystals of magnetite and are

not associated with any porosity in the magnetite structure (Deditius et al., 2018). The size of the inclusions ranges up to 400×100 nm for diopside, up to 100 nm for enstatite, 50×500 nm for amphibole, 200×20 – 40 nm for mica, and 20 to 100 nm for Fe-Ti oxides.

Actinolite chemistry and temperatures

Actinolite is intimately intergrown with, and paragenetically equivalent to, magnetite in all investigated samples from Los Colorados (Fig. 14). Though some samples contain up to

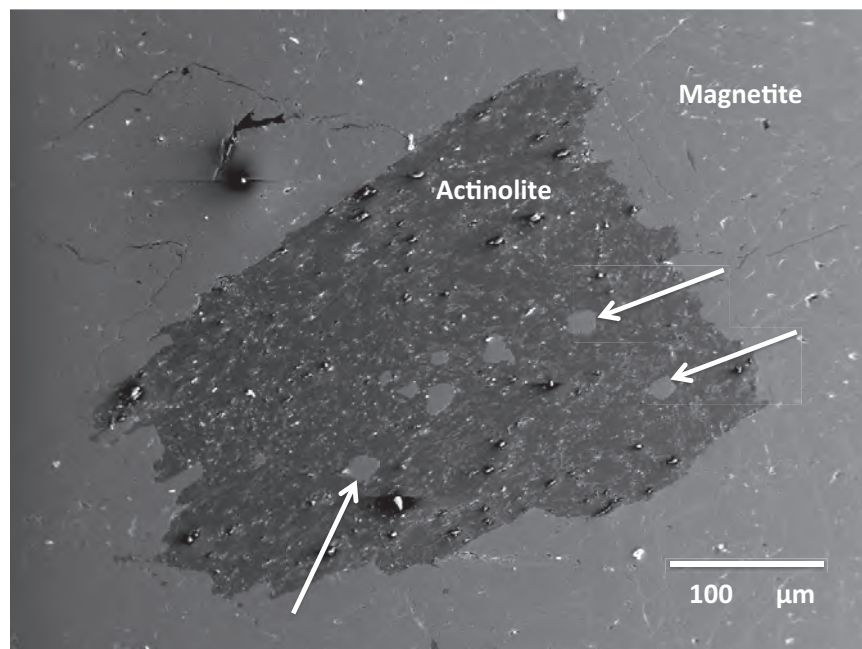


Fig. 14. Backscattered electron image of a representative actinolite grain intergrown with magnetite that is completely surrounded by magnetite. The white arrows point to magnetite grains within the actinolite grain. The sample is from drill core LC-05 in the Western orebody. Modified from Bilinker et al. (2016).

15 vol % actinolite, actinolite commonly occurs as a minor phase in most samples. The EPMA data for actinolite indicate that the Fe # ($\text{Fe\#} = [\text{molar Fe}]/[\text{molar Fe}] + [\text{molar Mg}]$) ranges from 0.35 to 0.44, with an average Fe # of 0.44 ± 0.28 (2σ) for all analyzed grains. The average Fe # for actinolite yields a model temperature of formation of 710° and 740°C at 100 and 200 MPa, respectively, following the methodology of Lledo and Jenkins (2008). The highest Fe # of 0.72 and lowest Fe # of 0.23 yield model temperatures of 620° and 810°C at 100 and 200 MPa, respectively. For detailed tables with EPMA and LA-ICP-MS data, see Bilenker et al. (2016).

Pyrite chemistry

Pyrite was analyzed in samples from the central part of the Western dike (i.e., drill core LC-05) and from the mineralized diorite intrusion. Pyrite in the Western dike occurs as disseminated grains (Fig. 15a, d, f) and veinlets (Fig. 15b, c, e). Pyrite is modally more abundant in the mineralized diorite where it occurs as disseminated grains and masses (Fig. 15d), in veinlets (Fig. 15e), and with magnetite and actinolite in stock-work-like assemblages. EPMA and SIMS analyses reveal that pyrite contains as much as 3.9 wt % Co and 1.5 wt % Ni, with a Co/Ni ratio >1 for almost all individual grains >1 , and Co/Ni

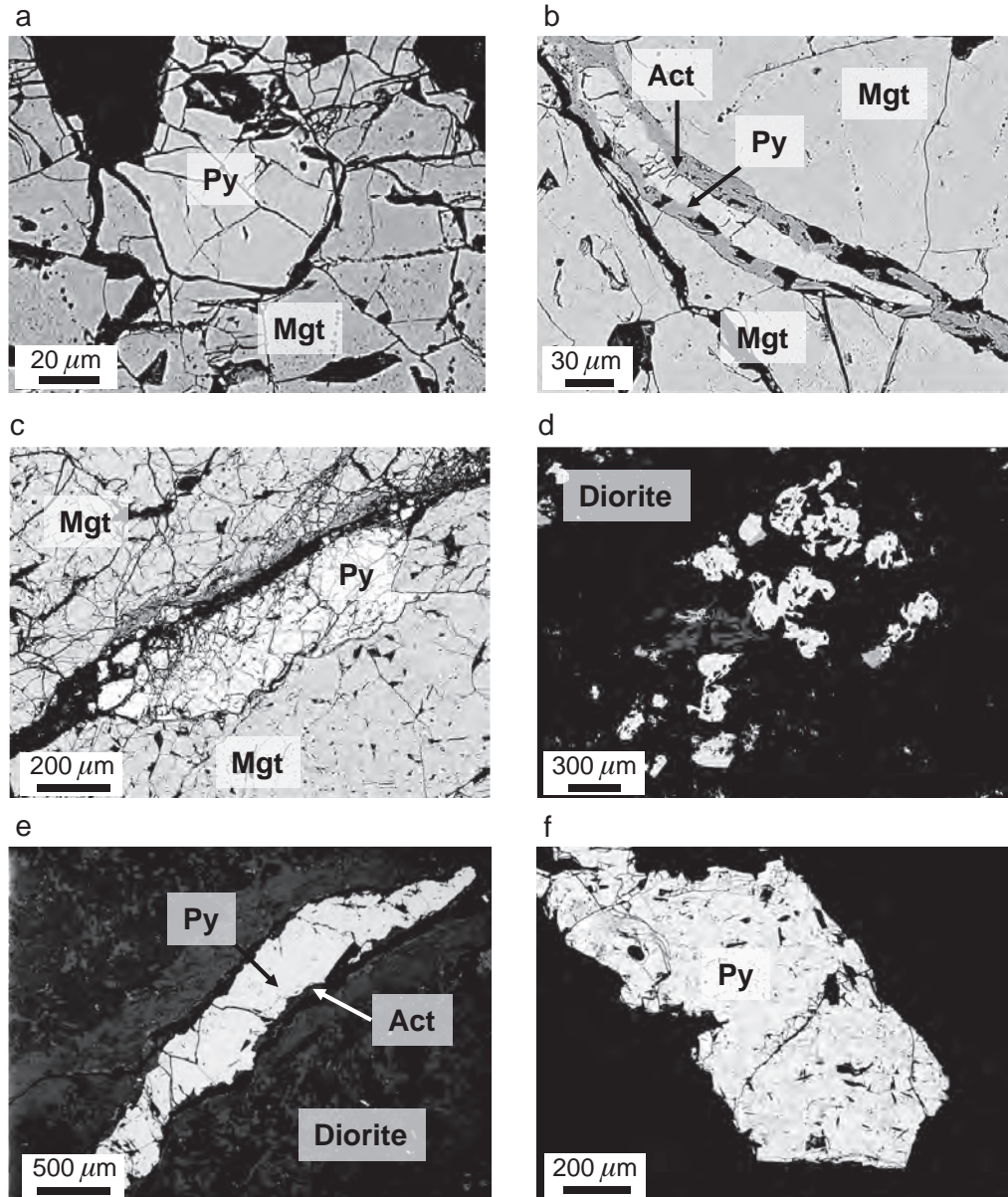


Fig. 15. Backscattered electron images of representative textural relationships of pyrite samples from Los Colorados. Pyrite occurs as disseminated grains (a, d, f) and in veinlets (b, c, e); both textural types occur in the massive magnetite orebodies, the ore breccias, and the diorite intrusion. Sulfide veinlets at Los Colorados are mostly monomineralic, where pyrite is associated with actinolite (b, e) and magnetite. Pyrite veinlets generally cut the magnetite ores in both the tabular orebodies (i.e., the magnetite dikes) and the diorite intrusive body, postdating the main magnetite stage defined by Ti-V-Al-Mn-rich cores (magnetite types 1 and 2, Knipping et al., 2015a, b). Abbreviations: Act = actinolite, Mgt = magnetite, Py = pyrite. From Reich et al. (2016).

> 2 for many grains (Fig. 16; Reich et al., 2016). The elevated Co/Ni ratios of pyrite imply precipitation of pyrite from an ore fluid evolved from an intermediate to mafic magma (Taylor et al., 1969). Pyrite grains exhibit oscillatory zoning with distinct zoning of Ni between Ni-rich and -poor bands. EPMA data indicate that the concentration of Cu in pyrite varies from ~100 ppb to ~1 wt %; however, SIMS depth profiles indicate that the highest Cu concentrations correlate with the presence of nanometer-sized Cu-bearing inclusions, most likely chalcopyrite. The EPMA and SIMS data reveal that the concentration of Au in pyrite varies from hundreds of ppb to ~800 ppm; however, the SIMS depth profiles reveal Au-enriched nanoparticles in pyrite that contaminate the EPMA signal. SIMS indicates that the concentration of Au dissolved in solid solution within the pyrite structure ranges from ~100 to ~30 ppm. The EPMA and SIMS data also record that Ag in pyrite varies from ~100 ppm to a maximum of ~30 ppm, with higher concentrations reflecting Ag-bearing nanoparticles. Arsenic in pyrite varies from 10s to ~2,000 ppm, whereas Sb, Se, and Te are each <100 ppm. The concentration of As in pyrite is positively correlated with both Cu and Au. The concentrations of Zn, Pb, and Cd vary from ~100 to 200, ~100 to 3,000, and ~100 to 400 ppm, and SIMS depth profiles do not

reveal nanoparticles enriched in any of these metals except for Te. The concentrations of all of the aforementioned trace elements are relatively constant within single pyrite grains, and are similar among all magnetite samples from the Western dike and the mineralized diorite. For detailed tables with EPMA and SIMS data, see Reich et al. (2016).

Oxygen isotopes in magnetite

Analyses of oxygen isotopes in magnetite from drill cores LC-04 (Western dike, Fig. 3) and LC-05 (western part of disseminated magnetite ore zone, Fig. 3), yield an average $\delta^{18}\text{O}$ value of 2.32 ± 0.12 and $2.76 \pm 0.12\text{‰}$, respectively, where $\delta^{18}\text{O}_{\text{sample}} (\text{‰}) = [((^{18}\text{O}/^{16}\text{O})_{\text{magnetite}} / (^{18}\text{O}/^{16}\text{O})_{\text{VSMOW}}) - 1] \times 1,000$. Samples were collected along about 120 m of drill core and these average values indicate minimal variation of $\delta^{18}\text{O}$ as a function of depth within the main orebody. In addition to magnetite samples from Los Colorados, we analyzed magnetite separates from the Kiruna-type Mariela IOA deposit in the Chilean iron belt (avg $\delta^{18}\text{O}$ value of $1.49 \pm 0.04\text{‰}$), the Pea Ridge and Pilot Knob Kiruna-type IOA deposits in Missouri, United States (avg $\delta^{18}\text{O}$ value of $4.14 \pm 1.86\text{‰}$ and $2.77 \pm 3.08\text{‰}$, respectively), the El Laco Kiruna-type IOA deposit in northern Chile (avg $\delta^{18}\text{O}$ value of $5.38 \pm 1.85\text{‰}$),

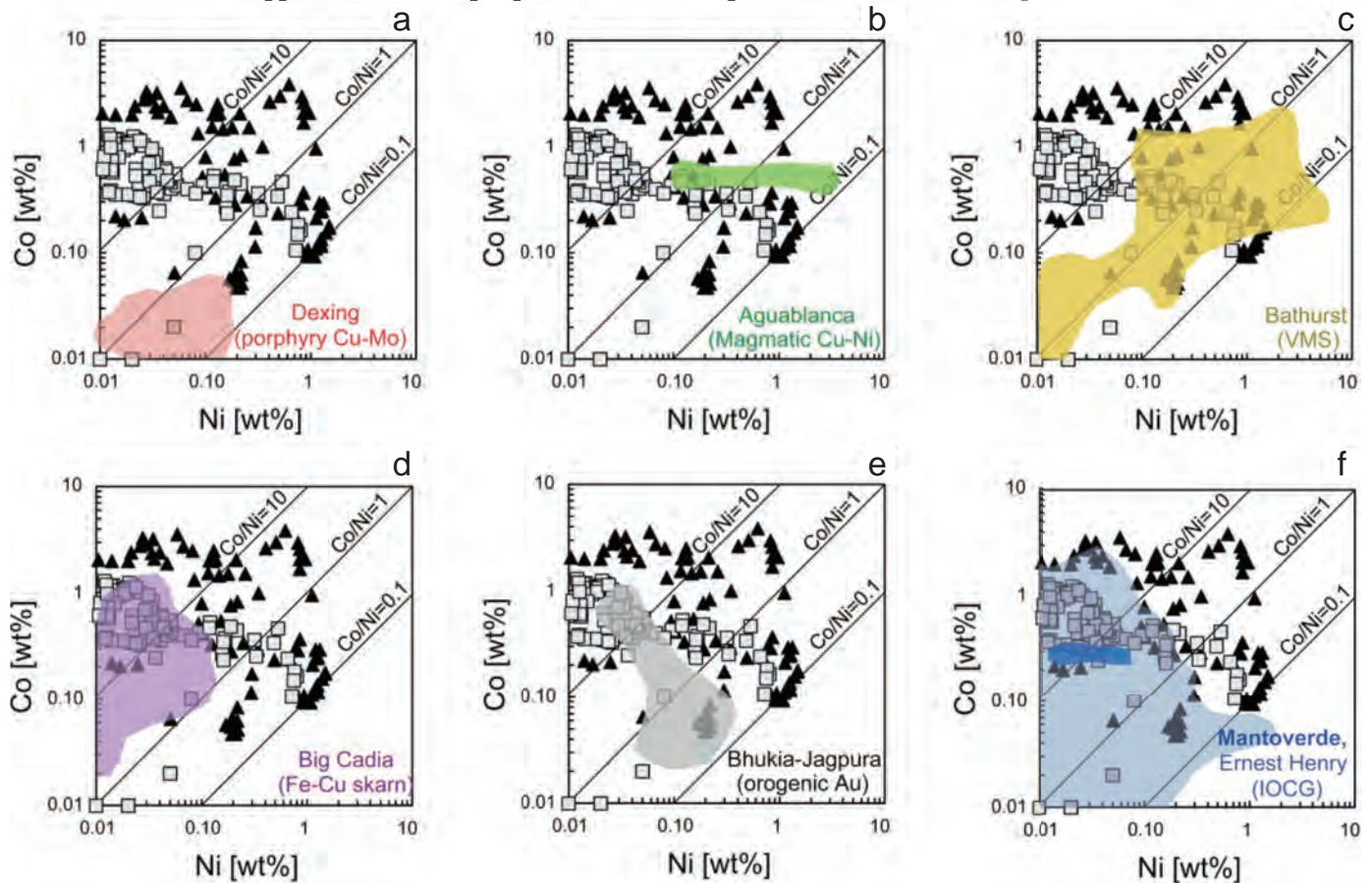


Fig. 16. The concentrations of Co vs. Ni in pyrite from Los Colorados. Squares are pyrite samples from the brecciated, mineralized diorite intrusion. Black triangles are for pyrite from the massive magnetite ore in the Western dike. The concentrations of Co vs. Ni for other deposits are shown as colored fields. (a). Dexing, China (porphyry Cu-Mo). (b). Aguablanca, Spain (magmatic Cu-Ni). (c). Bathurst district, Canada (VMS). (d). Big Cadia, Australia (Fe-Cu skarn). (e). Bhukia-Jagpura gold prospect, India (orogenic Au). (f). Ernest Henry, Australia, and Mantoverde, Chile (IOCG). Data sources: Bajwah et al. (1987), Rieger et al. (2010), Rusk et al. (2010), Deol et al. (2012), Piña et al. (2013), Reich et al. (2013), and Soltani Dehnavi et al. (2015). From Reich et al. (2016).

and the Kiirunavaara IOA deposit in Sweden (avg $\delta^{18}\text{O}$ value of $1.76 \pm 0.25\%$). We also analyzed magnetite separates from the Mantoverde IOCG deposit in the Chilean iron belt, which yield an average $\delta^{18}\text{O}$ value of $2.99 \pm 1.34\%$. All of the $\delta^{18}\text{O}$ data are plotted in Figure 17 along with ratios of $^{56}\text{Fe}/^{54}\text{Fe}$ relative to IRMM data that are presented in the next section. In Figure 17 are the fields for the global range of $\delta^{18}\text{O}$ values for igneous and magmatic-hydrothermal magnetite (Bilenker et al., 2016), a field indicating the range of nonmagmatic, low-temperature magnetite (e.g., banded iron formations), and a field that indicates the effects of postmineralization, hydrothermal alteration, which shifts $\delta^{18}\text{O}$ to lighter values. The field labeled magmatic and/or high-temperature origin represents every published $\delta^{18}\text{O}$ value for magnetite that crystallized from silicate melt or magmatic-hydrothermal fluid. All of the magnetite from Los Colorados plot in the magmatic and/or high-temperature origin box, as do the magnetite data from other Kiruna-type IOA deposits. Also plotted in Figure 17 are $\delta^{18}\text{O}$ values for magnetite from the Mantoverde IOCG deposit, which plot in the magmatic and/or high-temperature origin box. See Bilenker et al. (2016) for detailed data for samples from Chile and Sweden, Childress et al. (2016) for data for Pea Ridge and Pilot Knob, and Childress (writ. commun.) for data from Mantoverde.

Iron isotopes in magnetite

Analyses of stable iron isotopes in magnetite separates from drill cores LC-04 (Western dike) and LC-05 (northern and central part of the main orebody), the Western dike, yield an average $\delta^{56}\text{Fe}$ value of 0.29 ± 0.12 and $0.15 \pm 0.05\%$, respectively, where $\delta^{56}\text{Fe}_{\text{sample}} (\%) = [((^{56}\text{Fe}/^{54}\text{Fe})_{\text{magnetite}} / (^{56}\text{Fe}/^{54}\text{Fe})_{\text{IRMM-14}}) - 1] \times 1,000$. In addition to magnetite samples from Los Colorados, we analyzed magnetite separates from the Kiruna-type IOA Mariela deposit in the Chilean iron belt (two samples yield $\delta^{56}\text{Fe}$ values of 0.13 ± 0.03 and $0.57 \pm 0.04\%$; Bilenker et al., 2016), the Pea Ridge and Pilot Knob Kiruna-type IOA deposits in Missouri, United States (avg $\delta^{56}\text{Fe}$ value of 0.17 ± 0.10 and $0.18 \pm 0.07\%$, respectively; Childress et al., 2016), the El Laco Kiruna-type IOA deposit in northern Chile (average $\delta^{56}\text{Fe}$ value of $0.28 \pm 0.24\%$; Bilenker et al., 2016; Childress, writ. commun.), and the Kiirunavaara IOA deposit in Sweden ($\delta^{56}\text{Fe}$ value of $0.16 \pm 0.07\%$). We also analyzed magnetite separates from the Mantoverde IOCG deposit in the Chilean iron belt, which yielded an average $\delta^{56}\text{Fe}$ value of $0.48 \pm 0.08\%$. As with $\delta^{18}\text{O}$ presented above, the field labeled magmatic and/or high-temperature origin represents every published $\delta^{56}\text{Fe}$ value for magnetite that crystallized from silicate melt or magmatic-hydrothermal fluid. All of the magnetite from Los Colorados plot in the magmatic and/or high-temperature origin box, and the magnetite data from other Kiruna-type IOA deposits plot within the range of $\delta^{56}\text{Fe}$ consistent with magnetite crystallized from silicate melt or magmatic-hydrothermal fluid. Also plotted in Figure 17 are $\delta^{56}\text{Fe}$ values for magnetite from the Mantoverde IOCG deposit, all of which plot within the range of $\delta^{56}\text{Fe}$ consistent with magnetite crystallized from silicate melt or magmatic-hydrothermal fluid. The $\delta^{18}\text{O}$ values for Pea Ridge and Pilot Knob that are elevated relative to purely orthomagmatic magnetite are explained by Childress et al. (2016) to reflect crystallization of magnetite from a silicate

melt. See Bilenker et al. (2016) for detailed data for samples from Chile and Sweden, Childress et al. (2016) for data for Pea Ridge and Pilot Knob, and Childress et al. (writ. commun.) for data from Mantoverde.

Hydrogen isotopes in magnetite and actinolite

Analyses of actinolite yield a $\delta^{18}\text{O}$ value of $6.46 \pm 0.56\%$ and a δD value of $-59.3 \pm 1.7\%$. The water content of actinolite is 2.08 ± 0.04 wt %. Magnetite grains yield a δD value of $-53.5 \pm 1.5\%$, where $\delta\text{D}_{\text{sample}} (\%) = [((^2\text{H}/^1\text{H})_{\text{magnetite}} / (^2\text{H}/^1\text{H})_{\text{VSMOW}}) - 1] \cdot 1,000$. The water content of magnetite is 0.10 ± 0.07 wt %; the large uncertainty reflects the difficulty of measuring the small amount of water in magnetite grains. For details, see Bilenker et al. (2016).

Rhenium-Osmium systematics

Analyses of magnetite and pyrite separates from Los Colorados yielded concentrations of total Re that range from 0.71 to 128.76 ppb for magnetite, and 163.07 to 214.13 ppb for pyrite. Magnetite shows very low to negligible amounts of Os (0.2–1.0 ppt), whereas pyrite shows no detectable Os concentrations. A calculated model age for magnetite from Los Colorados, using the concentrations of ^{187}Os and ^{187}Re , yielded a 116.0 ± 6.2 Ma age, consistent with previously reported ages of 110 to 115 Ma for mineralization at Los Colorados (e.g., Pichon, 1981; Oyarzún and Frutos, 1984). The calculated initial $^{187}\text{Os}/^{188}\text{Os}$ ratio (Os_i) for magnetite from Los Colorados is 1.2. In addition, samples were analyzed from the Mantoverde (magnetite $\text{Os}_i = 2.1$), Candelaria (chalcopyrite $\text{Os}_i = 2.4$), and Diego de Almagro (pyrite $\text{Os}_i = 2.0$) IOCG deposits; the El Romeral (pyrite $\text{Os}_i = 1.0$) Kiruna-type deposit; and the Altamira Manto-type Cu deposit (chalcocite $\text{Os}_i = 1.1$). The calculated initial $^{187}\text{Os}/^{188}\text{Os}$ ratio for all of the aforementioned deposits is shown in Figure 18 along with the initial $^{187}\text{Os}/^{188}\text{Os}$ ratio for Chilean porphyry Cu deposits. The data indicate that the Os systematics from the Chilean IOA and IOCG deposits are statistically similar to the Os systematics for Chilean porphyry Cu deposits, a finding that supports that magmatic-hydrothermal processes were involved in the formation of the Chilean Kiruna-type deposits and IOCG deposits, as is unequivocally the case for the Chilean porphyry deposits. For details, see Barra et al. (2017).

A Novel Igneous and/or Magmatic-Hydrothermal Model

The magnetite-fluid flotation model

The major, minor, trace, isotopic, and textural data for magnetite samples from Los Colorados were used to scaffold a novel genetic model for the evolution of Kiruna-type deposits. The original model, published by Knipping et al. (2015a), invokes a synergistic combination of igneous and magmatic-hydrothermal processes to explain spatially and temporally related Kiruna-type IOA deposits and IOCG deposits as products of one evolving ore system (Fig. 2). Since that publication, the major, minor, trace, isotopic, and textural data subsequently collected for late-stage pyrite and magnetite from Los Colorados, as well as for samples from other Kiruna-type IOA deposits (i.e., Pea Ridge and Pilot Knob, both in Missouri, United States; El Laco, El Romeral, both in Chile; Kiruna, Sweden), and IOCG

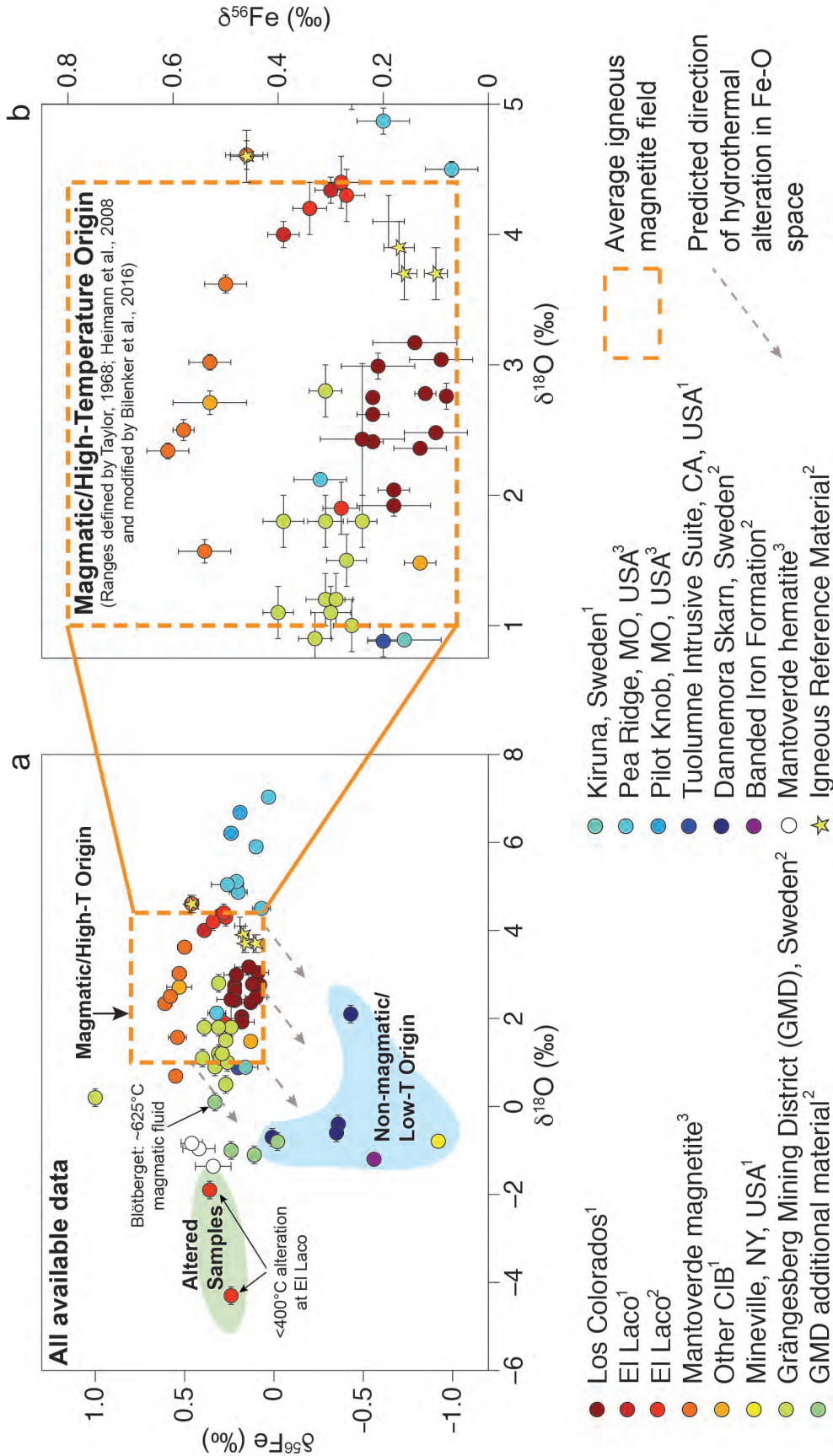


Fig. 17. Isotopic data for magnetite samples in $\delta^{56}\text{Fe}$ vs. $\delta^{18}\text{O}$ space. The dashed orange box denotes the range for magmatic (igneous) Fe and O isotope values as established by Taylor (1967, 1968), Heimann et al. (2008), Heimann et al. (2016, 2017), and Bilenker et al. (2013), and Bilenker et al. (2016, 2017). Stars denote $\delta^{56}\text{Fe}$ vs. $\delta^{18}\text{O}$ values for igneous magnetite reported by Weis (2013). Panel a displays all data discussed while panel b shows only datasets that include samples plotting within the igneous/high-temperature magmatic-hydrothermal $\delta^{56}\text{Fe}$ - $\delta^{18}\text{O}$ box. Error bars are 2σ . Data sources are indicated by superscripts as follows: 1 = Bilenker et al. (2016), 2 = Weis (2013), 3 = Childress et al. (2016). Mantoverde from Tristan Childress (writ. commun.). Samples labeled Grängesberg mining district (GMD) are magnetite from the massive magnetite-apatite orebody, whereas samples labeled GMD additional material are magnetite from the metavolcanic host rock. See Bilenker et al. (2016) for details.

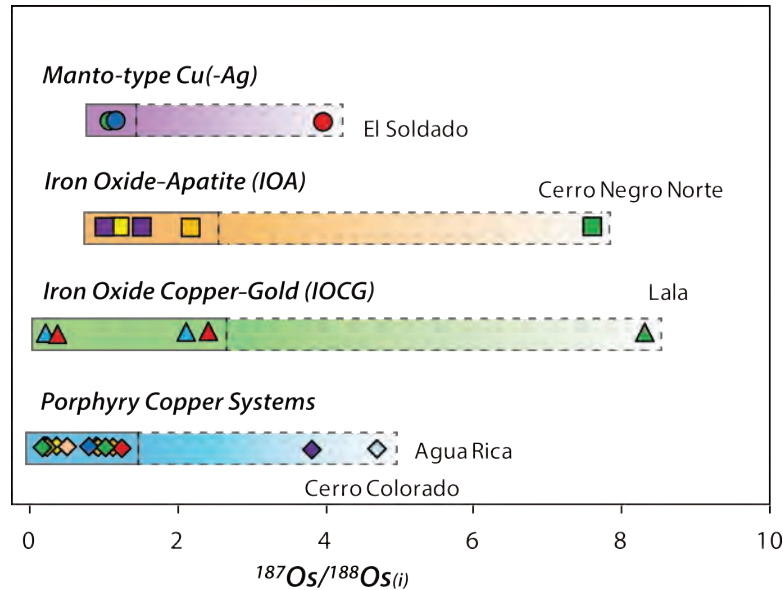


Fig. 18. The calculated initial Os ratios for Chilean Manto-type deposits, Kiruna-type deposits, and IOCG deposits are plotted along with initial Os ratios for samples from Andean porphyry Cu systems. The values for all ore deposit types overlap. More radiogenic values ($^{187}\text{Os}/^{188}\text{Os} > 3$) might be related to metals derived from sedimentary basins. Data from Mathur et al. (2002) and Barra et al. (2017). Data for Lala, China, from Zhimin and Yali (2013). See Barra et al. (2017) for discussion.

deposits (i.e., Mantoverde, Candelaria, Barreal Seco, Diego de Almagro; all in Chile) are at least in part consistent with the flotation model proposed by Knipping et al. (2015a).

In this new model, magnetite is a liquidus phase in a hydrous, oxidized arc magma, consistent with experimental phase equilibria studies of mafic to intermediate silicate magmas in an arc setting (Martel et al., 1999). According to Nadoll et al. (2014) and many other studies, igneous magnetite is enriched in trace elements such as Ti, Al, Mn, Cr, Ni, and Ga, consistent with the concentrations of these elements measured in the magnetite cores (i.e., type 1 magnetite) from the massive magnetite ores of Los Colorados (Figs. 9, 10). During ascent of a magnetite-saturated silicate magma, decompression decreases the solubility of fugitive components of the silicate melt (e.g., H_2O , CO_2) and can drive the melt to volatile saturation. As magmatic-hydrothermal fluid exsolves from the silicate melt, the exsolving fluid bubbles will nucleate on mineral surfaces in order to reduce surface energy (cf. Edmonds et al., 2014). The larger wetting angles (Ψ) between fluid and oxide minerals ($\Psi = 45^\circ\text{--}50^\circ$), when compared to fluid and silicate minerals ($\Psi = 5^\circ\text{--}25^\circ$; cf. Gualda and Ghiorso, 2007), results in fluid bubbles preferentially nucleating and attaching onto magnetite crystals rather than on silicate minerals (Hurwitz and Navon, 1994; Gardner and Denis, 2004; Cluzel et al. 2008). Thus, during decompression-induced fluid exsolution, bubbles will nucleate and grow on igneous magnetite crystals (Fig. 19).

The fluid-bubble pairs will ascend within the magma chamber owing to their positive buoyancy, consistent with experimental observations of sulfide melt droplets attached to fluid bubbles ascending through less dense silicate melt (Mungall et al., 2015) and segregation of chromite-bubble pairs in mafic magma (Matveev and Ballhaus, 2002). Buoyancy force calculations indicate that a magnetite-fluid suspension will

ascend in the parent magma chamber as long as the proportion of magnetite microlites in the suspension is < 65 wt % (< 37 vol %), which results in a $F^{\text{Buoyancy}} > 0$ (Knipping et al., 2015a). During ascent, the fluid component of the magnetite-bubble pairs will expand and become even less dense. This allows the bubbles to assimilate more magnetite crystals and form a fluid suspension rich in igneous magnetite. This is comparable to the “sweeping” process proposed by Edmonds et al. (2014) who invoked magnetite flotation by fluid bubbles to explain magnetite-rich mafic enclaves in arc andesite.

The abrupt change in the composition of magnetite from type 1 (core) to type 2 (rim) cannot be explained by progressive crystallization of magnetite from a silicate melt. Such an abrupt decrease in the concentration of trace elements such as Ti, Mn, and Al at the transition from type 1 to type 2 magnetite (Fig. 11), and the systematic decrease in the concentration of Ti, Mn, and Al from the type 1-type 2 interface toward the type 3 magnetite outer rim (Fig. 10), is consistent with type 2 magnetite rims having grown in the presence a cooling, aqueous fluid (Knipping et al. 2015b). This is based on the remarkable similarity between the magnetite compositions from Los Colorados and the global compilation of magnetite compositions from porphyry-type ore deposits reported in Nadoll et al. (2014; their fig. 12). The trend of decreasing trace element concentrations revealed by Figure 10 is consistent with growth of magnetite from aqueous fluid during cooling from $> 500^\circ$ to $< 200^\circ\text{C}$. Evidence for the presence of an aqueous fluid during magnetite growth at Los Colorados is preserved by the presence of magnetite-hosted, halite-saturated fluid inclusions (Fig. 7). It is well established that Cl-rich magmatic-hydrothermal fluids efficiently scavenge Fe from silicate melt as FeCl_2 (Simon et al., 2004; Bell and Simon, 2011), and that the concentration of Fe can exceed the concentration of other metals

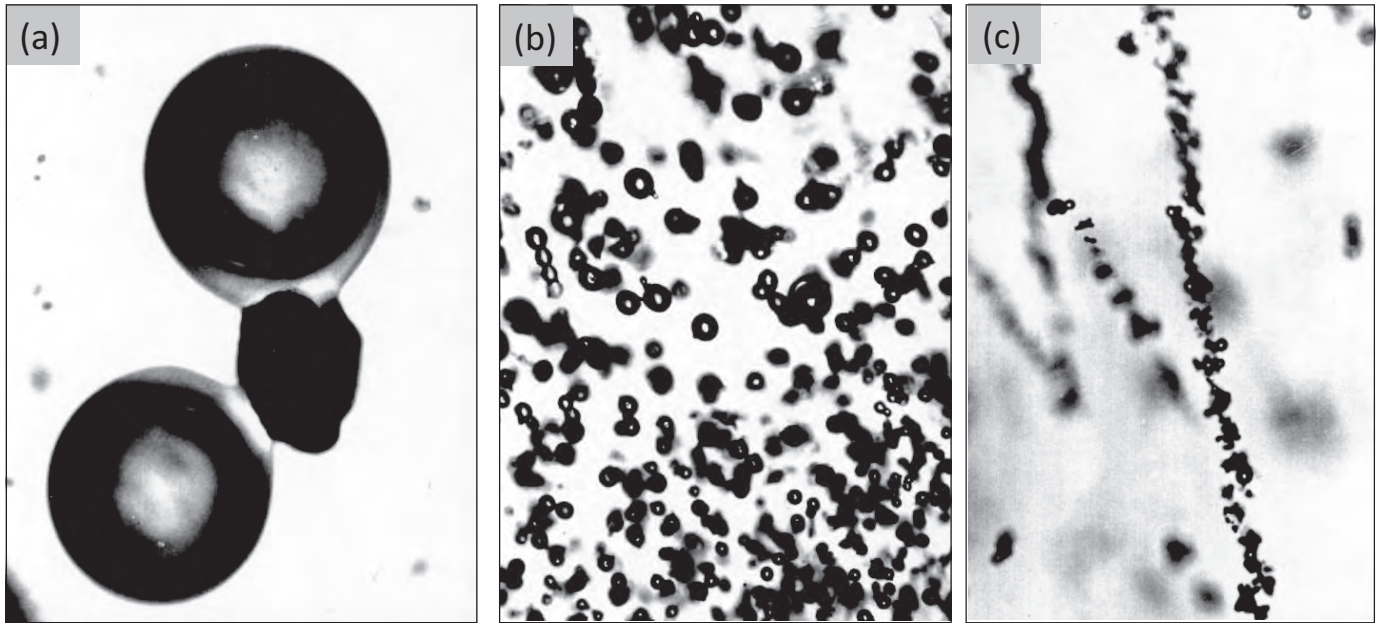


Fig. 19. Photomicrographs from experiments (Hurwitz, 1994; Hurwitz and Navon, 1994) that investigated bubble nucleation from a magnetite saturated silicate melt during decompression. Experiments were performed by decompressing an initially volatile-undersaturated, magnetite-saturated silicate melt from an initial pressure of 150 MPa to induce volatile saturation. In each of the three photographs, the white background is silicate glass (i.e., quenched silicate melt). (a). Decompression from 150 to 145 MPa resulted in volatile saturation of the melt. Two bubbles are attached to a single magnetite microlite. Both bubbles have a neck that extends toward the magnetite crystal. The radius of the bubbles is $\sim 25 \mu\text{m}$. (b). Same experiment as (a). An example of heterogeneous distribution of bubbles. The radius of the bubbles varies from ~ 8 to $\sim 30 \mu\text{m}$. The bubble density is $2 \times 10^7 \text{ cm}^{-3}$ in the lower portion of the photograph, where magnetite is abundant. The bubble density is $4 \times 10^6 \text{ cm}^{-3}$ in the upper portion of the photograph, where oxides are sparse. (c). Decompression from 150 to 120 MPa resulted in volatile saturation of the melt. The Fe-Ti oxide crystals and associated bubbles are all arranged along lines, following the spatial arrangement of magnetite grains in the starting material. Note that almost all bubbles are nucleated on magnetite crystal surfaces. The radius of the bubbles is $\sim 2 \mu\text{m}$. The photographs are from Hurwitz (1994).

dissolved in aqueous fluid (e.g., K, Na; Simon et al., 2004; Steele-MacInnis et al., 2015), especially in intermediate to mafic magmas (Bell and Simon, 2011). Thus, the fluid component of the fluid-magnetite suspension will be enriched in Fe, which allows the solute igneous magnetite to grow during decompression and/or cooling by sourcing Fe from the surrounding magmatic-hydrothermal fluid (Fig. 20). The overgrowth rims (i.e., type 2 magnetite) would have compositions consistent with magmatic-hydrothermal magnetite (cf. Nadoll et al., 2014).

Eventually, tectonic stress changes in the late Lower Cretaceous were responsible for the formation of the Atacama fault system in the back-arc setting. This transtensional, strike-slip, crustal scale fault system provides an ideal, structurally controlled, permeable conduit that allows the magnetite-rich suspension to ascend from the source magma. During ascent, magnetite in the fluid suspension will drop out of the suspension upon reaching a level of neutral buoyancy at shallow crustal depths, resulting in the massive, crosscutting, “dike-shaped” orebodies such as those observed at Los Colorados (Fig. 3). If the permeability of the host rocks is high, the fluid component of the suspension will percolate into the host rocks, resulting in disseminated and/or stockwork mineralization. As the percolating fluid continues to cool, this process should result in growth of magnetite from the fluid at progressively lower temperatures, as observed for the late-stage, hydrothermal magnetite at Los Colorados (Fig. 13). In summary, the

major features observed at Los Colorados are consistent with a model wherein a magnetite-fluid suspension evolves from an intermediate to mafic silicate magma and ascends toward the surface along preexisting crustal faults.

A critical feature of the model is that the presence of magnetite microlites in the ascending magmatic-hydrothermal fluid suspension allows for the formation of Kiruna-type IOA deposits from a smaller volume of magma, relative to formation from a conventional orthomagmatic fluid. For example, the $\sim 350 \text{ Mt}$ Fe at Los Colorados require a $\sim 50 \text{ km}^3$ magma chamber ($\sim 3.5 \text{ km}$ diameter) if a magnetite-fluid suspension that contains 8 wt % magnetite microlites evolves from the parent magma. This volume is within the range of arc volcano magma chambers ($\sim 4\text{--}60 \text{ km}^3$; Hildreth, 1981; Bacon, 1983; Marsh, 1989; Lipman, 1997; Caricchi et al., 2016) and in agreement with estimated caldera sizes of extrusive, Kiruna-type IOA deposits ($\sim 30 \text{ km}^2$; El Laco, Chile, Oyarzún and Frutos, 1984; Nyström and Henríquez, 1994). In contrast, formation of Los Colorados from a magnetite-free, orthomagmatic fluid, requires a magma volume of at least 100 km^3 , a volume higher than reported for most arc magma systems. Thus, incorporation of only a few weight percent magnetite microlites in the evolving ore fluid decreases significantly the source magma volume. Further, if the primary ore fluid was a magnetite-fluid suspension containing 8 wt % magnetite microlites, and the source magma was an intermediate andesitic composition, the fluid would scavenge only 0.4 wt % FeO

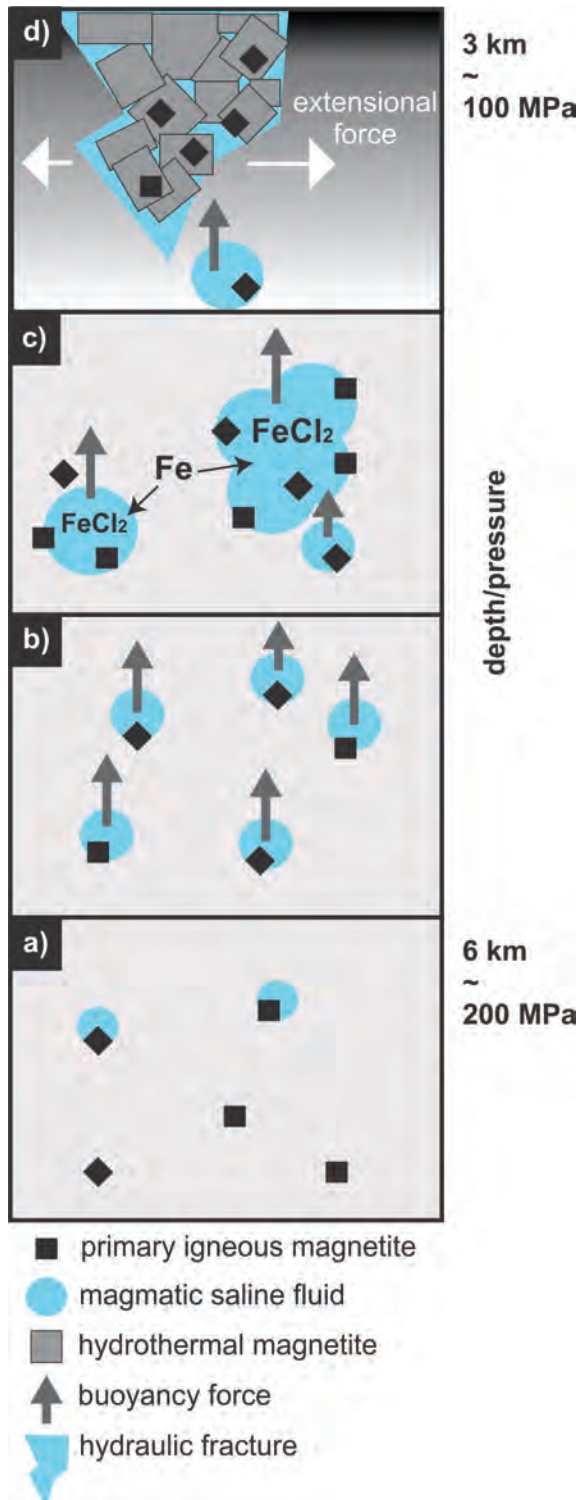


Fig. 20. The novel flotation model to explain the formation of Kiruna-type IOA deposits. (a). Magnetite saturation and preferred bubble nucleation on magnetite microlites that are 10's to $<200\text{-}\mu\text{m}$ diameter. (b). Ascension of bubble-magnetite pairs due to positive buoyancy forces. (c). Further ascent, growth, coalescence, and accumulation of primary magnetite as well as scavenging of Fe from the surrounding magmatic-hydrothermal fluid. (d). Formation of hydraulic fractures (due to tectonic stress changes) allows fast, efficient segregation of magnetite-rich fluid, and the growth of hydrothermal magnetite (gray overgrowth on primary magnetite microlites in top panel) during progressive cooling. Modified from Knipping et al. (2015b).

from the andesitic melt (Knipping et al., 2015a). Thus, from an exploration perspective, the composition of the source magma (pluton) would not be depleted in Fe. Importantly, postmineralization dissolution-reprecipitation may alter the primary signature of magnetite microlites, where immobile trace elements such as Ti originally dissolved in magnetite can form secondary titanite or rutile, as reported for the Kiruna-type, Pilot Knob IOA deposit (Nold et al., 2014), and is commonly observed in porphyry deposits (Berger et al., 2008). Thus, the absence of resolvable Ti-Al-Mn-enriched magnetite microlites in magnetite grains from Kiruna-type deposits is not evidence for their absence during mineralization.

Connecting Kiruna-type IOA and IOCG deposits

Deep drill core from IOCG deposits in the Chilean iron belt, e.g., Candelaria and Mantoverde, reveals that IOCG mineralization at shallow depth transitions to Kiruna-type IOA mineralization at deeper levels of individual deposits within these variable magmatic arc settings (Fig. 2). The flotation model described above explains the observations of a vertical continuum from IOCG to IOA mineralization, in contrast to the contradicting igneous hypothesis of liquid immiscibility between Fe- and Si-rich melts. According to model calculations by Knipping et al. (2015a), after Kiruna-type IOA mineralization, the further ascending ore fluid retains as much as 50% of the Fe initially dissolved in the fluid. The high Cl concentration of the fluid (Fig. 7) enhances the solubility of elements such as Fe, Cu, Au, P, REE, and Cr that partition strongly from the parent silicate melt into the primary magmatic-hydrothermal fluid (Eugster and Chou, 1979; Reed et al., 2000; Antignano and Manning, 2008; Klein-BenDavid et al., 2011; Watenphul et al., 2012; Zajacz et al., 2012; Migdisov et al., 2014; Hurtig and Williams-Jones, 2014; Williams-Jones and Migdisov, 2014). Hence, the magmatic-hydrothermal ore fluid has the ability to transport these elements into more distal crustal regions vertically and laterally, where they precipitate as oxides \pm sulfides \pm phosphates either through cooling alone ($T < 400^\circ\text{C}$; Hezarkhani et al., 1999; Ulrich et al., 2001; Hurtig and Williams-Jones, 2014; Williams-Jones and Migdisov, 2014), or possibly by mixing with cooler meteoric fluid, as discussed in Barton (2014).

The late-stage pyrite in the host rocks at Los Colorados is consistent with this model, as are experimental data for the transport of Cu and Au in Cl-bearing magmatic-hydrothermal fluid. The solubility maximum for Au in a cooling magmatic-hydrothermal fluid shifts to lower temperatures with decreasing density of the fluid (Hurtig and Williams-Jones, 2014). Those authors experimentally determined that Au solubility in an intermediate density fluid reaches a maximum at $\sim 500^\circ\text{C}$, whereas the solubility maximum is reached at $\sim 400^\circ\text{C}$ for a low density fluid. Experimental data for Cu are similar, revealing that the solubility maximum for Cu is reached at $\sim 600^\circ\text{C}$, and drops sharply once the fluid cools below 400°C (Migdisov et al., 2014; Williams-Jones and Migdisov, 2014). The solubility of Cu in the cooling magmatic-hydrothermal fluid also increases with increasing oxygen fugacity (Williams-Jones and Migdisov, 2014). Together, these data indicate that the ore fluid ascending from the zone of Kiruna-type mineralization (Fig. 2) will continue to transport Cu and Au, and that precipitation of Cu-Au-Fe sulfides will occur at shallow levels of the

system after the ore fluid cools below 400°C. The presence of hematite in the shallow regions of IOCG deposits is consistent with oxidation of the ascending ore fluid, which helps the fluid maintain high concentrations of Cu and Au.

Geochemical data for magnetite, hematite, and pyrite from the Mantoverde IOCG deposit in the Chilean iron belt, as well as other systems (Fig. 16) are consistent with a continuum from deep IOA mineralization to shallow IOCG mineralization over a depth of tens to hundreds of meters within the same ore-forming system. The $\delta^{56}\text{Fe}$ and $\delta^{18}\text{O}$ values for magnetite from Mantoverde indicate that both Fe and O were sourced from a magma reservoir (Fig. 17). The $\delta^{56}\text{Fe}$ values for hematite from Mantoverde also indicate that Fe is magmatically sourced. Hematite from Mantoverde yielded $\delta^{18}\text{O}$ values that range from -0.67 to -1.36‰ , consistent with $\delta^{18}\text{O}$ values reported by Benavides et al. (2007). The $\delta^{56}\text{Fe}$ values for hematite indicate a magmatic source, and the slightly negative $\delta^{18}\text{O}$ values of hematite are consistent with mixing of the dominantly magmatic ore fluid and a nonmagmatic fluid. The Co and Ni concentrations in pyrite from Mantoverde overlap those of pyrite from Los Colorados, and indicate derivation of Co and Ni from an intermediate to mafic magma (Fig. 16f). Published noble gas (Ar, Kr, Xe) and halogen (Cl, Br, I) compositions of fluid inclusions in hydrothermal quartz and calcite from the Mantoverde district also fingerprint a hypogene magmatic-hydrothermal fluid as the ore fluid (Marschik and Kendrick, 2015). Those authors report that Br/Cl and I/Cl ratios overlap those for the mantle and magmatic-hydrothermal

ore deposits, and low ^{36}Ar concentrations that reveal involvement of magmatic-hydrothermal fluid. Those authors concluded that the noble gas and halogen data are compatible with mixing of magmatic-hydrothermal fluids and evaporated seawater, which was modified by interaction with back-arc basin sediments. Perhaps most striking is a comparison of trace element concentrations in magnetite from Mantoverde with magnetite from Los Colorados (Fig. 21). Certainly, these deposits are not genetically related to each other, but considering that deep drill core at Mantoverde reveals that the deposit transitions with depth to a Kiruna-type IOA deposit, the data shown in Figure 21 illustrate the mineralization continuum expected for an ascending and evolving magnetite-fluid suspension.

The model described here also explains the modally minor amount of apatite and the depleted REE pattern for the massive magnetite ore at Los Colorados, when compared to the parallel but enriched REE pattern of the distal, brecciated diorite intrusion (Fig. 4). Precipitation of REE-rich apatite from cooling, magmatic, saline fluids within the surrounding wall rocks is in agreement with observations at the Kiirunavaara IOA deposit in Sweden, where also parallel, but strongly elevated REE patterns were detected in the hydrous altered host rocks when compared to the orebodies (Jonsson et al., 2013). Experimental data indicate that REE are dissolved dominantly as Cl complexes in aqueous fluid, and that cooling below 400°C is an efficient mechanism for precipitation of REE (Williams-Jones et al., 2012). Discharging of highly

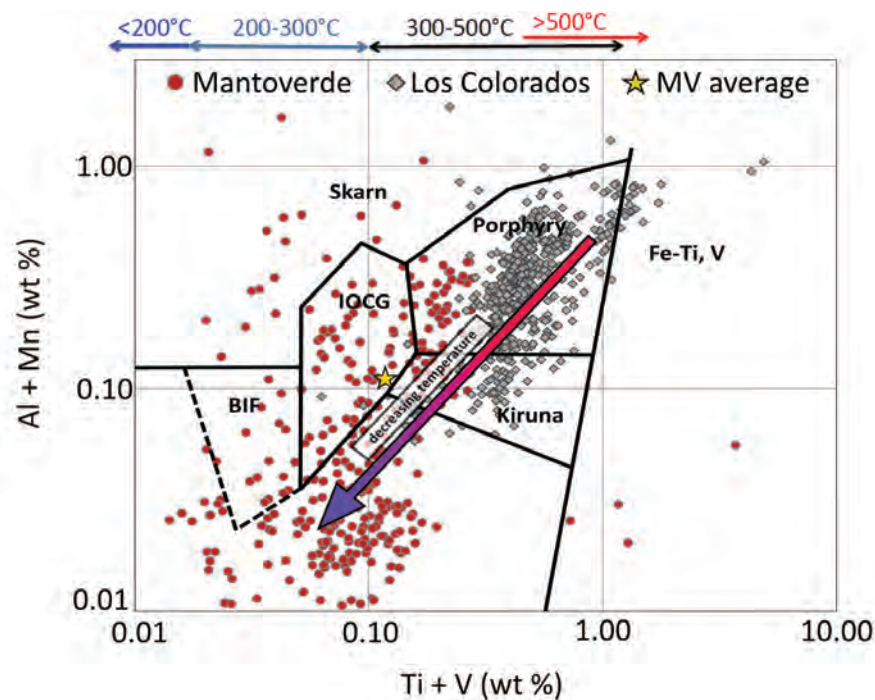


Fig. 21. The concentrations of $[\text{Al} + \text{Mn}]$ vs. $[\text{Ti} + \text{V}]$ for magnetite from the Mantoverde IOCG deposit in the Chilean iron belt are plotted in the magnetite trace element discrimination diagram from Nadoll et al. (2014), along with $[\text{Al} + \text{Mn}]$ vs. $[\text{Ti} + \text{V}]$ for magnetite from the Los Colorados Kiruna-type IOA deposit in the Chilean iron belt. Solid red circles and grey diamonds represent magnetite from Mantoverde and Los Colorados, respectively; data for Los Colorados from Knipping et al. (2015a). The yellow star indicates the average of all magnetite from Mantoverde. The temperatures on the top abscissa are from Nadoll et al. (2014) who compiled temperatures of magnetite crystallization in a variety of ore deposits. The color-graded arrow indicates the expected trend for the trace element chemistry of magnetite that grows from a cooling magmatic-hydrothermal fluid.

saline fluids after massive magnetite deposition may also explain the depletion of Cr in massive magnetite ore observed in many Kiruna-type IOA deposits (Loberg and Horndahl, 1983; Nyström and Henriquez, 1994; Core, 2004; Dupuis and Beaudoin, 2011; Dare et al., 2014, 2015). Chromium, which is highly mobile in high-temperature saline fluids (Klein-Ben-David, 2011; Watenphul et al., 2012) eludes the early stage of massive magnetite ore formation and precipitates later and distally from the main magnetite orebodies. This is not just consistent with the high Cr concentration detected in magnetite from the brecciated diorite intrusion distal from massive magnetite deposits of Los Colorados (Fig. 3), but also with the iron province in Missouri, United States. Almost no Cr (~2 ppm) was detected in magnetite from the Pea Ridge, Iron Mountain, and Pilot Knob IOA deposits, in contrast to the brecciated IOCG deposit Boss Bixby in the same district (Cr: 26 ppm; Kisvarsanyi and Proctor, 1967; Seeger, 2003; Nold et al., 2014).

Evidence from other systems for an igneous and/or magmatic-hydrothermal origin

Many excellent studies have been published recently that fingerprint a magmatic source for mineralizing fluids in Kiruna-type IOA and IOCG deposits in districts around the world.

Missouri IOA district: Hofstra et al. (2016) presented a wealth of geochemical data for samples from the Mesoproterozoic Pea Ridge IOA REE deposit in Missouri, United States, and conclude that a magmatic hydrothermal ore fluid evolved from a concealed mafic to intermediate-composition magma is the most plausible explanation for mineralization. Those authors did not find evidence for the presence of igneous magnetite microlites, but, as was pointed out above, dissolution-precipitation during the multiple postmineralization hydrothermal events (cf. King et al., 2008) that affected the Missouri deposits (and others) can eliminate the original igneous magnetite trace element signature. The conclusions reached by Hofstra et al. (2016) are consistent with those reached by Childress et al. (2016) who interpreted Fe and O stable isotope data for the Pea Ridge and Pilot Knob deposits in Missouri to indicate a magmatic source for the ore fluid in each deposit.

Kiruna IOA district: Jonsson et al. (2013) and Weis (2013) reported O and Fe stable isotope data for samples from Kiruna-type IOA deposits in the following districts in Sweden: Grängesberg, Kiruna, Ruotevare, Ulvön, Dannemora, Striberg, Tabeg. Those authors compare their data to O and Fe stable isotope compositions of orthomagmatic and hydrothermal magnetite from other mineral deposits and conclude that the most plausible explanation for the formation of the Kiruna-type IOA deposits in Sweden is precipitation of magnetite from a magmatic-hydrothermal fluid. The Fe and O isotope data reveal that magnetite mineralization in Kiruna-type ore deposits in the Grängesberg mining district occurred at temperatures from 600° to 900°C, consistent with temperatures of mineralization for the massive magnetite ore at Los Colorados (i.e., the Western dike) reported by Bilinker et al. (2016). Further, Weis (2013) reports that late-stage hydrothermal magnetite precipitated at temperatures below 400°C, also consistent with data for late-stage, hydrothermal, disseminated and veinlet magnetite from Los Colorados (Fig.

13). Westhues et al. (2016, 2017a, b) reported trace element, Lu-Hf, and Sm-Nd isotope data for whole rocks, zircon and monazite from mineralized samples from Paleoproterozoic Kiruna-type IOA deposits in the vicinity of Kiruna in northern Sweden. Those authors conclude that a magmatic-hydrothermal ore fluid is the most plausible explanation for the Kiruna-type IOA deposits.

Olympic Dam district: Oreskes and Einaudi (1992) presented fluid inclusion and oxygen isotope data for samples from the Acropolis deposit, a magnetite-rich deposit that is part of the Olympic Dam system. Their data indicate that a magmatic-hydrothermal ore fluid is the most plausible explanation for magnetite mineralization. Temperatures of mineralization for magnetite in the Acropolis deposit are ~400°C, consistent with the late-stage, hydrothermal magnetite at Los Colorados (Fig. 13). Oreskes and Einaudi (1992) also reported the presence of halite-saturated fluid inclusions that indicate salinities up to 42 wt % NaCl equiv, a finding also consistent with observations at Los Colorados (Knipping et al., 2015b). Wawryk (2017) reported Fe isotope data for samples from the Olympic Dam (Australia) IOCG system that are consistent with a magmatic source for Fe and, by inference, the ore-forming fluid that transported Fe and other metals and S into the ore depositional environment. The Wawryk (2017) study included samples from the “fresh” Roxby Downs Granite (drill hole RD2495), the altered Roxby Downs Granite from the “biotite-out” zone to the Hematite-Quartz barren core zone (RD2678, RD2749, RB224), Hillside, early magnetite-siderite-pyrite mineralization (RD2773, RU65-8320), chalcopyrite-hematite mineralization (RD1988, RD2749, RD2773, RU65-8230), massive hematite from Oak Dam, Acropolis and Wirrda Well, and late, coarse-grained specular hematite (WRD33, IDD7). Wawryk (2017) used Fe isotope data to calculate temperatures of mineralization for magnetite-pyrite pairs of ~580°C in samples from Hillside, consistent with minimum temperatures of ~580°C for magnetite mineralization at the Los Colorados IOA (Bilinker et al., 2016). Apukhtina et al. (2017) reported observations from deep drill core at Olympic Dam that reveal the presence of abundant, early magnetite and apatite at the deepest level of the mineralized system. The modally abundant magnetite mineralization extends from 1,516- to 2,329-m depth, more than 800 m of magnetite-rich mineralization, and the authors reported that it likely continues beneath the bottom of the drill hole. Apukhtina et al. (2017) reported that the textures are consistent with in situ brecciation and with mineralization caused by a hypogene, rapidly ascending magmatic-hydrothermal fluid. Finally, those authors also reported the sparse occurrence of fluorapatite, which is consistent with observations at Los Colorados as discussed above (cf. Knipping et al., 2015b).

Concluding Remarks

Field observations and geochemical and geochronological data from districts around the world reveal that IOCG deposits and Kiruna-type IOA deposits are commonly spatially and temporally associated with one another, as well as with igneous rocks that record magmatic activity contemporaneous with mineralization. These observations suggest that IOCG and Kiruna-type IOA deposit types may be

genetically related. The model described here, developed for deposits in the Andean arc setting, holistically explains the formation of IOCG and IOA deposits as a combination of common igneous and magmatic-hydrothermal processes that have operated across geologic time and informs our understanding of fundamental geochemical processes that occur in other tectonic settings. Certainly, there are differences among, and within, districts that host IOA and IOCG mineralization. It is to be expected that the geometry of, and connectivity within, fault systems that serve to structurally control ascent of the magnetite-fluid suspension, as well as local porosity-permeability of the host rocks, which controls lateral advection of the fluid following formation of Kiruna-IOA mineralization, play critical roles in the formation of IOA and IOCG deposits. The down-temperature gradient evolution of a magnetite-fluid suspension fully explains the salient geochemical features of some of the major IOCG and Kiruna-type IOA systems. Its application to various tectonic settings needs to be further explored. Lastly, it is critical to understand that postmineralization hydrothermal alteration likely obscures primary features. Thus, it is critical to view the flotation model described here through the lens of geologic time, tens to hundreds of millions of years of geologic activity that alter and mask primary mineralization. Our hope is that economic geologists will use observations and geochemical data from other IOCG-IOA systems to test and improve the flotation model that will lead to discovery of new ore deposits.

Acknowledgments

We thank Mario Rojo and Rodrigo Munizaga at CAP Minería for logistical support at the Los Colorados mine, and for providing access to hand and drill core samples. A.C.S. acknowledges the U.S. National Science Foundation for providing funding (EAR 1250239 and 152439). The Society of Economic Geologists is thanked for providing funding via student grants to J.K., L.B., and T.C. Funding for this study was provided to M.R. and F.B. by the MSI grant “Millennium Nucleus for Metal Tracing along Subduction” NC130065, FONDECYT grant 1140780, and FONDAP project 15090013 “Centro de Excelencia en Geotermia de Los Andes, CEGA.”

REFERENCES

- Antignano, A., and Manning C.E., 2008, Fluorapatite solubility in H₂O and H₂O-NaCl at 700 to 900°C and 0.7 to 2.0 GPa: *Chemical Geology*, v. 251, p. 112–119.
- Apukhtina, O.B., Kamenetsky, V.S., Ehrig, K., Kamenetsky, M.B., Maas, R., Thompson, J., McPhie, J., Ciobanu, C.L., and Cook, N.J., 2017, Early, deep magnetite-fluorapatite mineralization at the Olympic Dam Cu-U-Ag deposit, South Australia: *Economic Geology*, v. 112, p. 1531–1542.
- Bacon, C.R., 1983, Eruptive history of Mount Mazama and Crater Lake caldera, Cascade Range, U.S.A.: *Journal of Volcanology and Geothermal Research*, v. 18, p. 57–115.
- Bajwah, Z.U., Secombe, P.K., and Offler, R., 1987, Trace element distribution, Co:Ni ratios and genesis of the Big Cadia iron-ore deposit, New South Wales, Australia: *Mineralium Deposita*, v. 22, p. 292–300.
- Barra, F., Reich, M., Selby, D., Rojas, P., Simon, A.C., Salazar, E., and Palma, G., 2017, Unraveling the origin of the Andean IOCG clan: A Re-Os isotopes approach: *Ore Geology Reviews*, v. 81, p. 62–78.
- Barton, M.D., 2014, Iron oxide(-Cu-Au-REE-P-Ag-U-Co) systems: *Treatise on Geochemistry*, v. 13, p. 515–541.
- Barton, M.D., and Johnson, D.A., 1996, Evaporitic source model for igneous related Fe oxide-(REE-Cu-Au-U) mineralization: *Geology*, v. 24, p. 259–262.
- 2004, Footprints of Fe-oxide(-Cu-Au) systems: SEG 2004, Predictive Mineral Discovery Under Cover, University of Western Australia, Centre for Global Metallogeny Special Publication 33, p. 112–116.
- Bell, A., and Simon, A.C., 2011, Evidence for the alteration of the Fe³⁺/σ_{Fe} of silicate melt caused by the degassing of chlorine-bearing aqueous volatiles: *Geology*, v. 39, p. 499–502.
- Benavides, J., Kyser, T.K., Clark, A.H., Oates, C.J., Zamora, R., Tamovschi, R., and Castillo, B., 2007, The Mantoverde iron oxide-copper-gold district, III Región, Chile: The role of regionally derived, nonmagmatic fluids in chalcopyrite mineralization: *Economic Geology*, v. 102, p. 415–440.
- Berger, B.R., Ayuso, R.A., Wynn, J.C., and Seal, R.R., 2008, Preliminary model of porphyry copper deposits: U.S. Geological Survey Open-File Report 2008-1321, 55 p.
- Bilenker, L., Simon, A.C., Reich, M., Lundstrom, C., Bindeman, I., and Munizaga, R., 2016, Fe-O stable isotope pairs elucidate a high-temperature origin of Chilean iron oxide-apatite deposits: *Geochimica et Cosmochimica Acta*, v. 177, p. 94–104.
- Bilenker, L.B., Van Tongeren, J., Lundstrom, C.C., and Simon, A.C., 2017, Iron isotopic evolution during fractional crystallization of the uppermost Bushveld Complex layered mafic intrusion: *Geochemistry, Geophysics, Geosystems*, v. 18, p. 956–972.
- Brown, M., Díaz, F., and Grocott, F., 1993, Displacement history of the Atacama fault system 25°00′–27°00′S, northern Chile: *Geological Society of America Bulletin*, v. 105, p. 1165–1174.
- Caricchi, L., Simpson, G., and Schaltegger, U., 2016, Estimates of volume and magma input in crustal magmatic systems from zircon geochronology: the effect of modeling assumptions and system variables: *Frontiers in Earth Sciences*, v. 27, <https://doi.org/10.3389/feart.2016.00048>.
- CAP Annual Operating Summary 2016, <http://www.capmineria.cl/wp-content/uploads/2017/05/cap_mineria_anual_operating_summary_2016.pdf>.
- Chen H., Clark A.H., Kyser T.K., Ullrich T.D., Baxter R., Chen Y., and Moody T.C., 2010, Evolution of the Giant Marcona-Mina Justa iron oxide-copper-gold district, south-central Peru: *Economic Geology*, v. 105, p. 155–185.
- Chiaradia, M., Banks, D., Cliff, R., Marschik, R. and De Haller, A., 2006, Origin of fluids in iron oxide-copper-gold deposits: Constraints from δ³⁷Cl, ⁸⁷Sr/⁸⁶Sr and Cl/Br: *Mineralium Deposita*, v. 41, p. 565–573.
- Childress, T.M., Simon, A.C., Day, W.C., Lundstrom, C.C., and Bindeman, I.N., 2016, Iron and oxygen isotope signatures of the Pea Ridge and Pilot Knob magnetite-apatite deposits, southeast Missouri, USA: *Economic Geology*, v. 111, p. 2033–2044.
- Cluzel, N., Laporte, D. and Provost, A., 2008, Kinetics of heterogeneous bubble nucleation in rhyolitic melts: Implications for the number density of bubbles in volcanic conduits and for pumice textures: *Contributions to Mineralogy and Petrology*, v. 156, p. 745–763.
- Core, D.P., 2004, Oxygen and sulfur fugacities of granitoids: Implications for ore-forming processes: Doctoral dissertation, Ann Arbor, MI, University of Michigan, 245 p. <<https://deepblue.lib.umich.edu/handle/2027.42/124653>>
- Corriveau, L., 2007, Iron oxide copper gold (±Ag ±Nb, ±P ±REE ±U) deposits: a Canadian perspective: *Geological Association of Canada, Mineral Deposits Division, Special Publication 5*, 2007 p. 307–328.
- Dare, S.A.S., Barnes, S.-J., Beaudoin, G., Méric, J., Boutroy, E., and Potvin-Doucet, C., 2014, Trace elements in magnetite as petrogenetic indicators: *Mineralium Deposita*, v. 49, p. 785–796.
- Dare, S.A., Barnes, S.J., and Beaudoin, G., 2015, Did the massive magnetite “lava flows” of El Laco (Chile) form by magmatic or hydrothermal processes? New constraints from magnetite composition by LA-ICP-MS: *Mineralium Deposita*, v. 50, p. 607–617.
- Day, W.C., Slack, J.F., Ayuso, R.A., and Seeger, C.M., 2016, Regional geologic and petrologic framework for iron oxide ± apatite ± rare earth element and iron oxide copper-gold deposits of the Mesoproterozoic St. Francois Mountains terrane, southeast Missouri, USA: *Economic Geology*, v. 111, p. 1825–1858.
- Deditius, A., Reich, M., Simon, A.C., Suvorova, A., Knipping, J., Roberts, M.P., Rubanov, S., Dodd, A., and Saunders, M., 2018, Nanogeochemistry of hydrothermal magnetite: *Contributions to Mineralogy and Petrology*, 173:46, doi.org/10.1007/s00410-018-1474-1.
- Deol, S., Deb, M., Large, R.R., and Gilbert, S., 2012, LA-ICPMS and EPMA studies of pyrite, arsenopyrite and loellingite from the Bhukia-Jagpura gold prospect, southern Rajasthan, India: Implications for ore genesis and gold remobilization: *Chemical Geology*, v. 326–327, p. 72–87.
- Dupuis, C., and Beaudoin, G., 2011, Discriminant diagrams for iron oxide trace element fingerprinting of mineral deposit types: *Mineralium Deposita*, v. 46, p. 319–335.

- Edmonds, M., Brett, A., Herd, R.A., Humphreys, M.C.S., and Woods A., 2014, Magnetite-bubble aggregates at mixing interfaces in andesite magma bodies: Geological Society of London Special Publication 410, DOI 10.1144/SP410.7
- Espinoza, R.S, Véliz, G.H., Esquivel, L.J., Arias, F.J., and Moraga, B.A., 1996, The cupriferous province of the Coastal Range, northern Chile: Society of Economic Geologists Special Publication 5, p. 19–32.
- Eugster, H.P., and Chou, I.-M., 1979, A model for the deposition of Cornwall-type magnetite deposits: *Economic Geology*, v. 74, p. 763–774.
- Foose, M.P., and McLelland, J.M., 1995, Proterozoic low Ti iron oxide deposits in New York and New Jersey: Relation to Fe-oxide (Cu-U-Au-rare earth element) deposits and tectonic implications: *Geology*, v. 23, p. 665–668.
- Gardner, J.E. and Denis, M.-H., 2004, Heterogeneous bubble nucleation on Fe-Ti oxide crystals in high-silica rhyolite melts: *Geochimica et Cosmochimica Acta*, v. 68, 3587–3597.
- Groves, D.I., Bierlein, F.P., Meinert, L.D., and Hitzman, M.W., 2010, Iron oxide copper-gold (IOCG) deposits through Earth history: Implications for origin, lithospheric setting, and distinction from other epigenetic iron oxide deposits: *Economic Geology*, v. 105, p. 641–654.
- Gualda, G.A.R., and Ghiorsio, M.S., 2007, Magnetite scavenging and the buoyancy of bubbles in magmas. Part 2: Energetics of crystal-bubble attachment in magmas: *Contributions to Mineralogy and Petrology*, v. 154, p. 479–490.
- Haynes, D.W., 2000, Iron oxide copper (-gold) deposits—their position in the ore deposit spectrum and modes of origin, in Porter, T.M., ed., *Hydrothermal iron oxide copper-gold and related deposits: A global perspective: Adelaide, PGC Publishing*, v. 1, p. 71–90.
- Haynes, D.W., Cross, K.C., Bills, R.T., and Reed, M.H., 1995, Olympic Dam ore genesis: A fluid-mixing model: *Economic Geology*, v. 90, p. 281–307.
- Heimann, A., Beard, B.L. and Johnson, C.M., 2008, The role of volatile exsolution and sub-solidus fluid/rock interactions in producing high $^{56}\text{Fe}/^{54}\text{Fe}$ ratios in siliceous igneous rocks: *Geochimica et Cosmochimica Acta* 72, 4379–4396.
- Henríquez, F., Naslund H.R., Nyström, J.O., Vivallo, W., Aguirre, R., Dobbs, F.M., and Lledo, H., 2003, New field evidence bearing on the origin of the El Laco magnetite deposit, northern Chile—a discussion: *Economic Geology*, v. 98, p.1497–1500.
- Hezarkhani, A., Williams-Jones, A.E., and Gammons, C.H., 1999, Factors controlling copper solubility and chalcopyrite deposition in the Sungun porphyry copper deposit, Iran: *Mineralium Deposita*, v. 34, p. 770–783.
- Hildreth, W., 1981, Gradients in silicic magma chambers: Implications for lithospheric magmatism: *Journal of Geophysical Research*, v. 86, p. B10153–B10192
- Hitzman, M.W., 2000, Iron oxide-Cu-Au deposits: What, where, when, and why, in Porter, T.M., ed., *Hydrothermal iron oxide copper-gold and related deposits: A global perspective: Adelaide, PGC Publishing*, p. 9–26.
- Hitzman, M.W., Oreskes, N., and Einaudi, M.T., 1992, Geological characteristics and tectonic setting of Proterozoic iron oxide (Cu-U-Au-REE) deposits: *Precambrian Research*, v. 58, p. 241–287.
- Hofstra, A.H., Meighan, C.J., Song, X., Samson, I., Marsh, E.E., Lowers, H.A., Emsbo, P., and Hunt, A.G., 2016, Mineral thermometry and fluid inclusion studies of the Pea Ridge iron oxide-apatite-rare earth element deposit, Mesoproterozoic St. Francois Mountains terrane, southeast Missouri, USA: *Economic Geology*, v. 111, p. 1985–2016.
- Hou, T., Charlier, B., Holtz, F., Veksler, I., Thomas, R., Zhang, Z., and Namur, O., 2018, Immiscible hydrous Fe-Ca-P melt and the origin of iron oxide-apatite deposits: *Nature Communication*, 9:1415, doi:10.1038/s41467-018-03761-40.
- Hurtig, N.C., and Williams-Jones, A.E., 2014, An experimental study of the transport of gold through hydration of AuCl in aqueous vapour and vapour-like fluids: *Geochimica et Cosmochimica Acta*, v. 127, p. 305–325.
- Hurwitz, S., 1994, Bubble nucleation in rhyolitic melts: Experiments at high pressure, temperature, and water content: M.Sc. thesis, Hebrew University of Jerusalem, 102 p.
- Hurwitz, S., and Navon, O., 1994, Bubble nucleation in rhyolitic melts: Experiments at high pressure, temperature, and water content: *Earth and Planetary Science Letters*, v. 122, p. 267–280.
- Jonsson, E., Troll, V.R., Hoegdahl, K., Harris, C., Weis, F., Nilsson, K.P., and Skelton, A., 2013, Magmatic origin of giant “Kiruna-type” apatite-iron oxide ores in Central Sweden: *Nature Scientific Reports*, v. 3, p. 1644–1652.
- King, E.M., Trzaskus, A.P., and Valley, J.W., 2008, Oxygen isotope evidence for magmatic variability and multiple alteration events in the Proterozoic St. Francois Mountains, Missouri: *Precambrian Research*, v. 165, p. 49–60.
- Kisvarsanyi, G., and Proctor, P.D., 1967, Trace element content of magnetites and hematites, Southeast Missouri iron metallogenic province, USA: *Economic Geology*, v. 62, p. 449–471.
- Klein-BenDavid, O., Pettke, T., and Kessel, R., 2011, Chromium mobility in hydrous fluids at upper mantle conditions: *Lithos*, v. 125, p. 122–130.
- Knipping, J.L., Bilenker, L., Simon, A.C., Reich, M., Barra, F., Deditius, A., Lundstrom, C., Bindeman, I., and Munizaga, R., 2015a, Giant Kiruna-type deposits form by efficient flotation of magmatic magnetite suspensions: *Geology*, v. 43, p. 591–594.
- Knipping, J.L., Bilenker, L., Simon, A.C., Reich, M., Barra, F., Deditius, A., Wälle, M., Heinrich, C.A., Holtz, F., Munizaga, R., 2015b, Trace elements in magnetite from massive iron oxide-apatite deposits indicate a combined formation by igneous and magmatic-hydrothermal processes: *Geochimica et Cosmochimica Acta*, v. 171, p. 15–38.
- Lester, G.W., Clark, A.H., Kyser, T.K., and Naslund, H.R., 2013a, Experiments on liquid immiscibility in silicate melts with H₂O, P, S, F and Cl: Implications for natural magmas: *Contributions to Mineralogy and Petrology*, v. 166, p. 329–349.
- Lester, G.W., Kyser, T.K., and Clark, A.H., 2013b, Oxygen isotope partitioning between immiscible silicate melts with H₂O, P and S: *Geochimica et Cosmochimica Acta*, v. 109, p. 306–311.
- Lindsley, D.H. and Epler, N., 2017, Do Fe-Ti-oxide magmas exist? Probably not!: *American Mineralogist* 102, p. 2157–2169.
- Lipman, P.W., 1997, Subsidence of ash-flow calderas: Relation to caldera size and magma-chamber geometry: *Bulletin of Volcanology*, v. 59, p. 198–218.
- Loberg, E.H., and Horndahl, A.-K., 1983, Ferride geochemistry of Swedish Precambrian iron ores: *Mineralium Deposita* v. 18, p. 487–504.
- Lledo, H.L., and Jenkins, D.M., 2008, Experimental investigation of the upper thermal stability of Mg-rich actinolite implications for Kiruna-type iron deposits: *Journal of Petrology*, v. 49, p. 225–238.
- Martel, C., Pichavant, M., Holtz, F. and Scaillet, B., 1999, Effects of f_{O_2} and H₂O on andesite phase relations between 2 and 4 kbar: *Journal of Geophysical Research*, v. 104, p. 29,453–29,470.
- Marschik, R., and Kendrick, M.A., 2015, Noble gas and halogen constraints on fluid sources in iron oxide-copper-gold mineralization: Mantoverde and La Candelaria, northern Chile: *Mineralium Deposita*, v. 50, p. 357–371.
- Marsh, B.D., 1989, Magma chambers: *Annual Reviews of Earth and Planetary Science*, v. 17, p. 439–474.
- Matveev, S., and Ballhaus, C., 2002, Role of water in the origin of podiform chromitite deposits: *Earth and Planetary Science Letters*, v. 203, p. 235–243.
- Ménard, J.J., 1995, Relationship between altered pyroxene diorite and the magnetite mineralization in the Chilean iron belt, with emphasis on the El Algarrobo iron deposits (Atacama region, Chile): *Mineralium Deposita*, v. 30, p. 268–274.
- Migdisov, A.A., Bychkov, A.Y., Williams-Jones, A.E., and van Hinsberg, V.J., 2014, A predictive model for the transport of copper by HCl-bearing water vapour in ore-forming magmatic-hydrothermal systems: Implications for copper porphyry ore formation: *Geochimica Cosmochimica Acta*, v. 129, p. 33–53.
- Mumin A.H., Corriveau L., Somarin A.K., and Ootes L., 2007, Iron oxide copper-gold-type polymetallic mineralization in the Contact Lake belt, Great Bear magmatic zone, Northwest Territories, Canada: *Exploration and Mining Geology*, v. 16, p. 187–208.
- Mungall, J.E., Brenan, J.M., Godel, B., Barnes, S.J., and Gaillard, F., 2015, Transport of metals and sulphur in magmas by flotation of sulphide melt on vapour bubbles: *Nature Geoscience*, v. 8, p. 216–219.
- Nadoll, P., Angerer, T., Mauk, J.L., French, D., and Walshe, J., 2014, The chemistry of hydrothermal magnetite: A review: *Ore Geology Reviews*, v. 61, p. 1–32.
- Naslund, H.R., Henríquez, F., Nyström, J.O., Vivallo, W., and Dobbs, F.M., 2002, Magmatic iron ores and associated mineralisation: Examples from the Chilean High Andes and coastal Cordillera, in Porter, T.M., ed., *Hydrothermal iron oxide copper-gold and related deposits: A global perspective: Adelaide, PGC Publishing*, v. 2, p. 207–226.
- Nold, J.L., Dudley, M.A., and Davidson, P., 2014, The southeast Missouri (USA) Proterozoic iron metallogenic province—types of deposits and genetic relationships to magnetite-apatite and iron oxide-copper-gold deposits: *Ore Geology Reviews*, v. 57, p. 154–171
- Nyström, J.O., and Henríquez, F., 1994, Magmatic features of iron ores of the Kiruna type in Chile and Sweden: Ore textures and magnetite geochemistry: *Economic Geology*, v. 89, p. 820–839.

- Oreskes, N., and Einaudi, M.T., 1992, Origin of hydrothermal fluids at Olympic Dam: Preliminary results from fluid inclusions and stable isotopes: *Economic Geology*, v. 87, p. 64–90.
- Oyarzún, J., and Frutos J., 1984, Tectonic and petrological frame of the Cretaceous iron deposits of north Chile: *Mining Geology*, v. 34, p. 21–31.
- Oyarzún, R., Oyarzún, J., Ménard, J.J., and Lillo, J., 2003, The Cretaceous iron belt of northern Chile: Role of oceanic plates, a superplume event, and a major shear zone: *Mineralium Deposita*, v. 38, p. 640–646.
- Park, C.F., Jr., 1961, A magnetite “flow” in northern Chile: *Economic Geology*, v. 56, p. 431–436.
- Pichon, R., 1981, Contribution à l'étude de la ceinture du fer du Chili. Les gisements de Bandurrias (Prov. d'Atacama) et Los Colorados Norte. (Prov. de Huasco): Thesis, University of Paris, 326 p.
- Piña, R., Gervilla, F., Barnes, S.-J., Ortega, L., and Lunar, R., 2013, Platinum-group elements-bearing pyrite from the Aguablanca Ni-Cu sulphide deposit (SW Spain): A LA-ICP-MS study: *European Journal of Mineralogy*, v. 25, p. 241–252.
- Pincheira, M., Thiele, R., and Fontbote, L., 1990, Tectonic transpression along the southern segment of the Atacama fault zone, Chile: *Colloques et Séminaires: Symposium International Géodynamique, Andine, Grenoble*, p. 133–136.
- Pollard, P.J., 2006, An intrusion-related origin for Cu-Au mineralization in iron oxide-copper-gold (IOCG) provinces: *Mineralium Deposita*, v. 41, p. 179–187.
- Reed, M.J., Candela, P.A., and Piccoli, P.M., 2000, The distribution of rare earth elements between monzogranitic melt and the aqueous volatile phase in experimental investigations at 800°C and 200 MPa: *Contributions to Mineralogy and Petrology*, v. 140, p. 251–262.
- Reich, M., Deditius, A., Chrystosoulis, S., Li, J.W., Ma, C.Q., Parada, M.A., Barra, F., and Mittermayr, F., 2013, Pyrite as a record of hydrothermal fluid evolution in a porphyry copper system: A SIMS/EMPA trace element study: *Geochimica et Cosmochimica Acta*, v. 104, p. 42–62.
- Reich, M., Simon, A.C., Deditius, A., Barra, F., Chrystosoulis, S., Lagas, G., Tardani, D., Knipping, J., Bilenker, L., Sanchez-Alfaro, P., Roberts, M.P., and Munziga, R., 2016, Trace element signature of pyrite from the Los Colorados iron oxide-apatite (IOA) deposit, Chile: A missing link between Andean IOA and iron oxide-copper-gold systems?: *Economic Geology*, v. 111, p. 743–761.
- Rhodes, A.L., and Oreskes, N., 1999, Oxygen isotope composition of magnetite deposits at El Laco, Chile: Evidence of formation from isotopically heavy fluids: *Society of Economic Geologists Special Publication 7*, p. 333–351.
- Rhodes, A.L., Oreskes, N., and Sheets, S., 1999, Geology and REE geochemistry of the magnetite deposits at El Laco, Chile: *Economic Geology Special Publication 7*, p. 299–332.
- Rieger, A.A., Marschik, R., Diaz, M., Hölzl, S., Chiaradia, M., Akker B., and Spangenberg, J.E., 2010, The hypogene iron oxide copper-gold mineralization in the Mantoverde district, northern Chile: *Economic Geology*, v. 105, p. 1271–1299.
- Rojas, P.A., Barra, F., Reich, M., Deditius, A., Simon, A.C., Uribe, F., Romero, R., and Rojo, M., 2018, A genetic link between magnetite mineralization and diorite intrusion at the El Romeral iron oxide-apatite deposit, northern Chile: *Mineralium Deposita*, <https://doi.org/10.1007/s00126-017-0777-x>.
- Ruiz, F.C., and Ericksen, G.E., 1962, Metallogenic provinces of Chile, S.A.: *Economic Geology*, v. 57, p. 91–106.
- Rusk, B.G., Oliver, N.H.S., Cleverley, J.S., Blenkinsop, T.G., Zhang, D., Williams, P.J., and Habermann, P., 2010, Physical and chemical characteristics of the Ernest Henry iron oxide copper gold deposit, Australia: Implications for IOCG genesis, in Porter, T.M., ed., *Hydrothermal iron oxide copper-gold and related deposits: A global perspective*: Adelaide, PGC Publishing, v. 3, p. 201–218.
- Scheuber, E., and Andriessen, P., 1990, The kinematic and geodynamic significance of the Atacama fault zone, northern Chile: *Journal of Structural Geology*, v. 12, p. 243–257.
- Seeger, C.M., 2000, Southeast Missouri iron metallogenic province: Characteristics and chemistry, in Porter, T.M., ed., *Hydrothermal iron oxide copper-gold and related deposits: A global perspective*: Adelaide, PGC Publishing, v. 1, p. 237–248.
- 2003, Lithology and alteration assemblages of the Boss iron-copper deposit, Iron and Dent Counties, Southeast Missouri: Doctoral dissertation, University of Missouri, 139 p. <http://scholarsmine.mst.edu/doctoral_dissertations/1473>.
- Sillitoe, R.H., 2003, Iron oxide-copper-gold deposits: An Andean view: *Mineralium Deposita*, v. 38, p. 787–812.
- Sillitoe, R.H., and Burrows, D.R., 2002, New field evidence bearing on the origin of the El Laco magnetite deposit, northern Chile: *Economic Geology*, v. 97, p. 1101–1109.
- Simon, A.C., Pettke, T., Candela, P.A., Piccoli, P.M., and Heinrich, A.H., 2004, Magnetite solubility and iron transport in magmatic-hydrothermal environments: *Geochimica et Cosmochimica Acta*, v. 68, p. 4905–4914.
- Soltani Dehnavi, A., Lentz, D.R., and McFarlane, C.R.M., 2015, LA-ICPMS analysis of volatile trace elements in massive sulphides and host rocks of selected VMS deposits of the Bathurst mining camp, New Brunswick: Methodology and application to exploration: *Geological Survey of Canada Open File 7853*, 214 p.
- Steele-MacInnis, M., Lecumberri-Sanchez, P., and Bodnar, R.J., 2015, Synthetic fluid inclusions XX. Critical PTX properties of H₂O-FeCl₂ fluids: *Geochimica et Cosmochimica Acta*, v. 148, p. 50–61.
- Sun, S.-S., and McDonough, W. F., 1989, Chemical and isotopic systematics of oceanic basalts: Implications for mantle composition and processes: *Geological Society [London] Special Publication 42*, p. 313–345.
- Taylor, S.R., Kaye, M., White, A.J.R., Duncan, A.R., and Ewart, A., 1969, Genetic significance of Co, Cr, Ni, Sc and V content of andesites: *Geochimica et Cosmochimica Acta*, v. 33, p. 275–286.
- Taylor, H.P., 1967, Oxygen isotope studies of hydrothermal mineral deposits, in Barnes, H.L., ed., *Geochemistry of hydrothermal ore deposits*, 1st ed.: New York, Holt, Rinehart and Winston, p. 109–142.
- 1968, The oxygen isotope geochemistry of igneous rocks: *Contributions to Mineralogy and Petrology*, v. 19, p. 1–71.
- Tornos, F., Velasco, F., and Hanchar, J.M., 2016, Iron-rich melts, magmatic magnetite, and superheated hydrothermal systems: The El Laco deposit, Chile: *Geology*, v. 44, p. 427–430.
- 2017, The magmatic to magmatic-hydrothermal evolution of the El Laco deposit (Chile) and its implications for the genesis of magnetite-apatite deposits: *Economic Geology*, v. 112, p. 1595–1628.
- Travisany, V., Henriquez, F., and Nyström, J.O., 1995, Magnetite lava flows in the Pleito-Melon district of the Chilean iron belt: *Economic Geology*, v. 90, p. 438–444.
- Ulrich, T., Günther, D., and Heinrich, C.A., 2001, The evolution of a porphyry Cu-Au deposit, based on LA-ICP-MS analysis of fluid inclusions: Bajo de la Alumbrera, Argentina: *Economic Geology*, v. 96, p. 1743–1774.
- Uyeda, S., and Kanamori, H., 1979, Back-arc opening and the mode of subduction: *Journal of Geophysical Research*, v. 84, p. 1049–1061.
- Velasco, R., Tornos, F., and Hanchar, J.M., 2016, Immiscible iron- and silica-rich melts and magnetite geochemistry at the El Laco volcano (northern Chile): Evidence for a magmatic origin for the magnetite deposits: *Economic Geology*, v. 79, p. 346–366.
- Watenphul, A., Schmidt, C., and Scholten, L., 2012, First insights into Cr³⁺ solubility in aqueous fluids at elevated P and T by μ -XRF [abs.]: *European Mineralogical Conference*, 1st, Frankfurt, Germany, Abstract 544, <<http://meetingorganizer.copernicus.org/EMC2012/EMC2012-544.pdf>>.
- Wawryk, C., 2017, An investigation into iron isotope systematics in felsic magmas and their associated magmatic-hydrothermal ore deposits: PhD. dissertation, University of Adelaide, Australia.
- Weis, F., 2013, Oxygen and iron isotope systematics of the Grängesberg mining district (GMD), Central Sweden: M.S. thesis, Uppsala universitet, <<https://www.diva-portal.org/smash/get/diva2:589233/FULLTEXT01.pdf>>.
- Westhues, A., Hanchar, J.M., Whitehouse, M.J., and Martinsson, O., 2016, New constraints on the timing of host-rock emplacement, hydrothermal alteration, and iron oxide-apatite mineralization in the Kiruna district, Norrbotten, Sweden: *Economic Geology*, v. 111, p. 1595–1618.
- Westhues, A., Hanchar, J.M., LeMessurier, M.J., and Whitehouse, M.J., 2017a, Evidence for hydrothermal alteration and source regions for the Kiruna iron oxide-apatite ore (northern Sweden) from zircon Hf and O isotopes: *Geology*, v. 45, p. 571–574.
- Westhues, A., Hanchar, J.M., Voisey, C.R., Whitehouse, M.J., Rossman, G.R., and Wirth, R., 2017b, Tracing the fluid evolution of the Kiruna iron oxide apatite deposits using zircon, monazite, and whole rock trace elements and isotopic studies: *Chemical Geology*, v. 466, 303–322.
- Williams, P.J., Barton, M.D., Johnson, D.A., Fontboté, L., de Haller, A., Mark, G., Oliver, N.H.S., and Marschik, R., 2005, Iron oxide copper-gold deposits: Geology, space-time distribution, and possible modes of origin: *Economic Geology 100th Anniversary Volume*, p. 371–405.

- Williams-Jones, A.E., and Migdisov, A.A., 2014, Experimental constraints on the transport and deposition of metals in ore-forming hydrothermal systems: Society of Economic Geologists Special Publication 18, p. 77–95.
- Williams-Jones, A.E., Migdisov, A.A., and Samson, I.M., 2012, Hydrothermal mobilisation of the rare earth elements—a tale of “Ceria” and “Yttria.” *Elements*, v. 8, p. 355–360.
- Zajacz, Z., Candela, P.A., Piccoli, P.M., Wälle, M., and Sanchez-Valle, C., 2012, Gold and copper in volatile saturated mafic to intermediate magmas: Solubilities, partitioning, and implications for ore deposit formation: *Geochimica et Cosmochimica Acta*, v. 91, p. 140–159.